

Interactive Multiscale Modeling to Bridge Atomic Properties and Electrochemical Performance in Li-CO₂ Battery Design

Mohammed Lemaalem ^{a,b}, Selva Chandrasekaran Selvaraj ^{a,b}, Ilias Papailias ^c,
Naveen K. Dandu ^{a,b}, Arash Namaeighasemi^a, Larry A. Curtiss^b, Amin
Salehi-Khojin ^c, and Anh T. Ngo ^{a,b,*}

^a *Department of Chemical Engineering, University of Illinois Chicago, Chicago, IL60608, USA*

^b *Materials Science Division, Argonne National Laboratory, Lemont, IL 60439, USA.*

^c *Department of Mechanical Engineering, Lyle School of Engineering, SMU, 3101 Dyer Street Dallas, TX 75205, USA*

Abstract

Li-CO₂ batteries show promise as energy storage solutions, offering high theoretical energy density and CO₂ fixation. Their performance relies on the formation and decomposition of Li₂CO₃/C during discharge and charge cycles, respectively. We used a multiscale modeling framework that integrates Density Functional Theory (DFT), Ab-Initio Molecular Dynamics (AIMD), classical Molecular Dynamics (MD), and Finite Element Analysis (FEA) to investigate atomic and cell-level properties. The Li-CO₂ battery consists of a lithium metal anode, an ionic liquid electrolyte, and a carbon cloth porous cathode with a Sb_{0.67}Bi_{1.33}Te₃ catalyst. DFT and AIMD determined the electrical conductivities of Sb_{0.67}Bi_{1.33}Te₃ and Li₂CO₃ using the Kubo-Greenwood formalism and studied the CO₂ reduction mechanism on the cathode catalyst. MD simulations calculated the CO₂ diffusion coefficient, Li⁺ transference number, ionic conductivity, and Li⁺ solvation structure. The FEA model, incorporating results from atomistic simulations, reproduced experimental voltage-capacity profiles at 1 mA/cm² and revealed spatio-temporal variations in Li₂CO₃/C deposition, porosity, and CO₂ concentration dependence on discharge rates in the cathode. Accordingly, Li₂CO₃ can form toroidal and thin film deposits, leading to dispersed and local porosity changes at 0.1 mA/cm² and 1 mA/cm², respectively. The capacity decreases exponentially from 81,570 mAh/g at 0.1 mA/cm² to 6,200 mAh/g at 1 mA/cm², due to pore clogging that limits CO₂ transport to the cathode interior. Therefore, the performance of Li-CO₂ batteries can be significantly improved by enhancing CO₂ transport, regulating Li₂CO₃ deposition, and optimizing cathode architecture.

*anhngo@uic.edu, angot@anl.gov

1. Introduction

Lithium-carbon dioxide (Li-CO₂) batteries, with their high theoretical energy density and CO₂ fixation capability, have emerged as a potential energy storage solution [1, 2]. These batteries provide a theoretical specific energy density of 1876 Wh kg⁻¹, which is substantially higher than that of current lithium-ion battery systems [3, 4]. This high energy density makes Li-CO₂ batteries particularly attractive for applications in aviation, aerospace, and electric vehicles, where lighter and more compact energy storage solutions are crucial [5]. The potential for electric vehicles with much longer ranges or considerably lighter batteries could revolutionize the automotive market [6, 5]. However, Li-CO₂ batteries are still in early development stages and face challenges including reaction reversibility issues, low energy efficiency, and the need for improved cathode designs [7]. Ongoing research and development efforts focus on overcoming these limitations, with recent advancements showing promising results [4, 8, 9, 10, 11, 12, 13, 14]. The Li-CO₂ batteries operate on a unique electrochemical principle involving the reversible reaction between lithium and carbon dioxide [1, 2] contributing to CO₂ capture and utilization efforts [11, 15]. During the discharge process, lithium oxidizes at the anode, releasing lithium ions and electrons ($Li \rightarrow Li^+ + e^-$). Besides, at the cathode in the presence of solid catalysts [16, 4], CO₂ undergoes reduction ($3CO_2 + 4e^- \rightarrow 2CO_3^{2-} + C$), combining with lithium ions and electrons to form primarily lithium carbonate (Li₂CO₃) and carbon (C) ($4Li^+ + 3CO_2 + 4e^- \rightarrow 2Li_2CO_3 + C$). This discharge reaction typically occurs at a voltage of approximately 2.8 V [17]. The charging process reverses these reactions, decomposing the discharge products to regenerate lithium and CO₂. However, due to the stability of Li₂CO₃, this process requires higher voltages, often exceeding 3.8 V [18]. This voltage requirement highlights one of several key challenges facing Li-CO₂ battery technology. The formation of solid Li₂CO₃ and carbon can lead to electrode clogging and increased internal resistance [9, 19]. The high charging voltages necessary for Li₂CO₃ decomposition reduce overall energy efficiency [20, 21]. Effective cathode catalysts are critical for enhancing reaction kinetics and minimizing overpotentials in Li-CO₂ batteries [8, 22]. Unwanted side reactions, particularly electrolyte decomposition, can occur at high voltages [7]. Furthermore, the inherent inertness of CO₂ makes its electrochemical reduction challenging, affecting discharge voltage and efficiency [23, 2, 15].

The Li-CO₂ battery chemistry faces critical challenges in catalyst performance, primarily characterized by two fundamental issues, catalyst inefficiency and redox mediator limitations. Noble and transition metal catalysts (such as Pt and Au nanoparticles) demonstrate low catalytic activities for CO₂ reduction/evolution reactions in aprotic media, while 2D materials (e.g., MoS₂) exhibit poor structural stability at high current rates [18]. Existing catalysts struggle to maintain consistent performance across multiple charge-discharge

cycles, often due to catalyst deactivation caused by self-degradation or environmental factors such as discharge product accumulation and species contamination [18]. Unlike Li-O₂ batteries, Li-CO₂ battery liquid catalysts are typically inactive in decomposing discharge products (Li₂CO₃ and solid carbon), and current redox mediators fail to effectively facilitate the reversible transformation of reaction intermediates [24]. The formation of Li₂CO₃, a wide-bandgap insulator, leads to slow kinetics and high voltage platforms (>4.3 V) during the charging process, significantly decreasing the round-trip efficiency of the battery [25]. The lack of efficient decomposition mechanisms significantly impedes battery cycling efficiency, with most current Li-CO₂ batteries only capable of operating for dozens of cycles with low overpotential, even with state-of-the-art catalysts [18]. These challenges necessitate developing novel catalytic systems that can maintain high catalytic activity across extended cycling, demonstrate structural stability at elevated current rates, enable efficient decomposition of discharge products, and provide reversible electrochemical reactions with minimal energy loss. The development of catalysts with high catalytic activity and conductivity is crucial to the research of high-performance Li-CO₂ batteries [22]. Promising research directions in Li-CO₂ battery technology encompass a range of innovative approaches aimed at overcoming current limitations and enhancing overall performance [26, 25, 27]. Advanced solid redox mediators have shown significant potential, as demonstrated by a study using a Cu(II) coordination compound of benzene-1,3,5-tricarboxylic acid. This solid redox mediator enabled a Li-CO₂ battery to achieve a higher discharge voltage of 2.8 V, a lower charge potential of 3.7 V, and superior cycling performance over 400 cycles [26]. The use of solid redox mediators addresses the shuttle effect and sluggish kinetics associated with soluble redox mediators, potentially improving long-term stability and efficiency. Alternative reaction pathway engineering has emerged as another promising direction, focusing on promoting the formation of Li₂C₂O₄ instead of Li₂CO₃ as the discharge product. This approach can reduce the charge potential and improve overall battery performance [25]. For instance, the use of Mo₂C as a cathode material has been shown to stabilize Li₂C₂O₄ as the final discharge product, reducing the charge potential to 3.8 V and enhancing the reversibility of the battery [25]. Innovative catalyst designs, including carbon-based and metal-complex catalysts, are being extensively explored. Carbon-based materials, such as multi-walled carbon nanotubes (MWCNTs), are widely used as cathodes due to their high electrical conductivity and large surface area [27]. However, their limited catalytic activity for Li₂CO₃ decomposition has led to investigations of ways to enhance their performance, such as introducing metal catalysts like Ru to reduce overpotentials and improve efficiency [27]. Transition metal compound catalysts have shown promise in improving the catalytic activity and stability of Li-CO₂ batteries. For example, the integration of Ru-catalyzed MWCNT cathodes with solid electrolytes has demonstrated enhanced electrochemical reactions involving CO₂ [27]. Additionally, nanostructured catalyst development with improved conductivity and catalytic properties continues to be a focus area, exploring various materials and structures to optimize battery performance [4, 10, 11].

Ionic liquid-based electrolytes show promise for Li-CO₂ batteries due to their stability with intermediate products compared to solid-state electrolytes, but their development is limited by low ionic conductivity and high viscosity [18]. To address these limitations, ionic liquid electrolytes based on DMSO (dimethyl sulfoxide) as a solvent and LiTFSI (lithium bis(trifluoromethanesulfonyl)imide) as a salt, often incorporating EMIM-BF₄ (1-Ethyl-3-methylimidazolium tetrafluoroborate), have been developed [28, 29, 30, 31, 3, 32, 4]. These electrolytes are preferred for Li-CO₂ batteries due to their superior ionic conductivity, enhanced electrochemical stability, and improved CO₂ activation properties. DMSO-based electrolytes exhibit faster Li⁺ ion diffusion kinetics compared to other solvents like TEGDME (tetraethylene glycol dimethyl ether), resulting in lower polarization potential [28]. Li-CO₂ batteries using 3M LiTFSI in DMSO electrolyte have demonstrated excellent cycling performance, maintaining stable operation for over 1,900 hours (180 cycles) [28]. In concentrated DMSO-based electrolytes, TFSI⁻ anions can access the primary solvation sheath of Li⁺ ions, leading to the formation of a LiF-rich solid electrolyte interphase (SEI) layer, which is beneficial for battery performance [29, 30]. DMSO-based electrolytes demonstrate good electrochemical stability with both the Li metal anode and the reactive cathode at high voltages and elevated temperatures [28]. The use of DMSO-based electrolytes improves the rate capability of the battery, with cells able to deliver flat charge/discharge plateaus at current densities of up to 2,000 mA g⁻¹ [29]. Together, these properties make the DMSO LiTFSI electrolyte a promising choice for improving the overall performance and stability of Li-CO₂ batteries. The addition of EMIM-BF₄ (1-Ethyl-3-methylimidazolium tetrafluoroborate) as an electrolyte material plays several important roles in Li-CO₂ batteries. EMIM-BF₄ helps in activating CO₂ molecules, which is crucial for the CO₂ reduction reaction in Li-CO₂ batteries [31]. The addition of EMIM-BF₄ to the electrolyte has been shown to enhance battery performance. In one study, a Li-CO₂ battery using 0.1 M LiTFSI in (EMIM-BF₄)/DMSO as the electrolyte achieved 500 cycles at 0.5 A/g with a capacity of 500 mAh/g [28]. The presence of EMIM-BF₄ in the electrolyte contributes to improved cycling stability of Li-CO₂ batteries [3]. When combined with other electrolyte components like DMSO and LiTFSI, EMIM-BF₄ contributes to the overall performance enhancement of Li-CO₂ batteries, including higher discharge voltages and increased capacities [32]. Recently, Jaradat et al. used an electrolyte combination of ZnI₂, LiTFSI, DMSO, and EMIM-BF₄ with a volumetric ratio of 2:3 that led to good Li-CO₂ battery performance [4].

Although recent research has focused on novel cathode materials and electrolytes to improve Li-CO₂ battery cell performance [10, 33, 34, 11, 14, 13, 35], most computational work has focused primarily on atomistic-level or continuum-level modeling. There is a critical need for a comprehensive multiscale approach that bridges these disparate levels of analysis to provide a more holistic understanding of batteries [36, 37, 38, 39]. To address this gap, we present an interactive multiscale modeling framework for Li-CO₂ batteries that integrates

density functional theory (DFT), ab initio molecular dynamics (AIMD), classical molecular dynamics (MD), and finite element analysis (FEA) in a coordinated manner. This approach bridges the atomic properties and electrochemical performance of Li-CO₂ batteries.

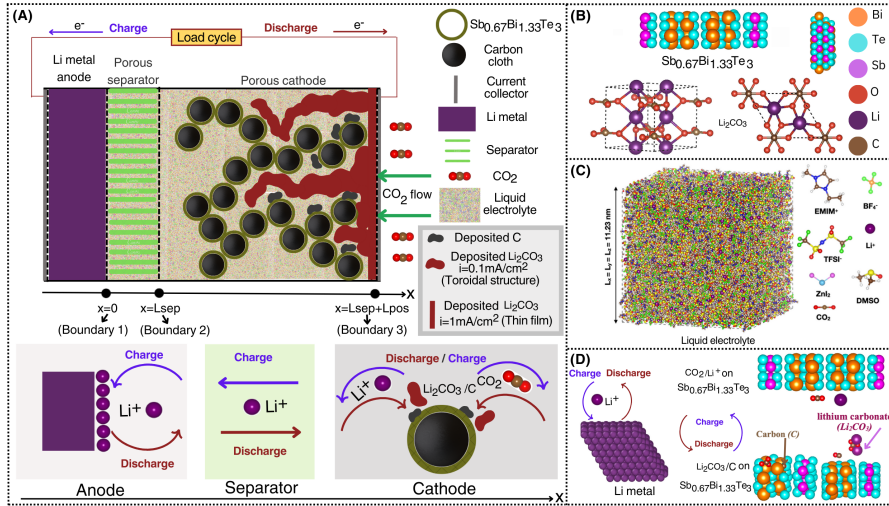


Figure 1: Multiscale modeling of Li-CO₂ battery cell from atomistic detail to component-level description. (A) Schematic diagram of the Li-CO₂ battery cell model used in FEA. (B) Ball and stick models of unit-cell structures of Sb_{0.67}Bi_{1.33}Te₃ optimized geometry from DFT calculation, with projection of unit-cell structures [100] and [001], and Li₂CO₃ with projection of unit-cell structures [110] and [001]. (C) Snapshot of MD simulation of the liquid electrolyte equilibrated under room temperature and ambient pressure (T=300K, P=1bar). (D) Anode and cathode reactions at the atomistic level, (left) Lithium oxidation/reduction of Lithium ions at the atomistic level, (right) Li₂CO₃/C formation/decomposition on Sb_{0.67}Bi_{1.33}Te₃ surface.

At the Li-CO₂ battery cell level, Finite Element Analysis (FEA) effectively simulates charge/discharge cycles, enabling macroscopic analysis of complex processes within the battery cell. These processes include ion transport through porous electrodes, reaction kinetics, and their impact on cell performance [40, 41, 42]. However, FEA requires accurate electrode and electrolyte properties as input parameters, which can be derived from atomistic simulations. At the atomic scale, classical Molecular Dynamics (MD) simulations excel in estimating transport properties such as diffusion coefficients and ionic conductivity in battery electrolytes [43, 44]. Complementing this approach, the combination of Density Functional Theory (DFT) and Ab Initio Molecular Dynamics (AIMD) enables the calculation of electrode electrical conductivity and reaction rate coefficients at the electrolyte/electrode interface [45, 12, 46, 47].

To bridge the gap between atomic and cell-level simulations, we first employ

DFT/AIMD calculations to determine the electrical conductivity of Li_2CO_3 and $\text{Sb}_{0.67}\text{Bi}_{1.33}\text{Te}_3$ using the Kubo-Greenwood formula [48, 49, 50], as well as to study the surface reaction of Li_2CO_3 as cathode catalyst material. Secondly, we conducted large-scale MD simulations to investigate the transport properties of the liquid electrolyte. Specifically, we calculate the diffusion coefficients of Li^+ and CO_2 , and the Li^+ transference number by examining the mean square displacement (MSD) of the particles over time using the Einstein equation [51], and the ionic conductivity using the Green-Kubo formula [52]. Finally, the atomic-scale insights gained from DFT/AIMD and MD simulations are then integrated into our FEA model, allowing for a comprehensive analysis of cell-level performance. Our FEA simulations investigate various aspects of battery cell behavior, including specific capacity, discharge behavior, and voltage-capacity profiles considering factors such as CO_2 transport properties, cathode porosity, and deposition of Li_2CO_3 and carbon. The studied Li- CO_2 battery cell consists of a lithium anode, an ionic liquid electrolyte, and a porous cathode. The electrolyte consists of a mixture of 1-ethyl-3-methylimidazolium tetrafluoroborate (EMIM- BF_4) and dimethyl sulfoxide (DMSO) in a 2:3 ratio, supplemented with zinc iodide (ZnI_2) and 1 M lithium bis(trifluoromethanesulfonyl)imide (LiTFSI) salt. This specific electrolyte composition has been experimentally demonstrated to yield optimal battery cell performance [4]. The cathode uses carbon cloth functionalized with a stable transition metal trichalcogenide alloy catalyst ($\text{Sb}_{0.67}\text{Bi}_{1.33}\text{Te}_3$), improving CO_2 reduction and oxidation kinetics [4]. This multiscale approach enables us to make predictions about porosity, deposited species quantities, and CO_2 concentration variations-parameters that are difficult to assess through experimental methods alone. Furthermore, it allows us to evaluate these properties as a function of time, providing dynamic insights into the battery’s behavior. This computational methodology can be used to test and screen various battery materials, potentially saving significant time and resources by reducing the need for extensive experimental tests.

2. Methods and computational details

2.1. Density Function Theory calculations (DFT) for structure optimization

We performed first-principles-based Density Functional Theory (DFT) calculations to optimize the crystal structures of $\text{Sb}_{0.67}\text{Bi}_{1.33}\text{Te}_3$ and Li_2CO_3 compounds using the Vienna Ab-initio Simulation Package (VASP) [53, 54]. The $\text{Sb}_{0.67}\text{Bi}_{1.33}\text{Te}_3$ structure is constructed based on the Sb_2Te_3 structure from the Materials Project database [55]. Multiple possible structures for $\text{Sb}_{0.67}\text{Bi}_{1.33}\text{Te}_3$ were optimized, and the most energetically favorable configuration (i.e., with the lowest optimization energy) is presented in Figure 1 (B). The Li_2CO_3 structure presented in 1B is obtained from the Materials Project database [55]. The projector augmented wave (PAW) formalism described the valence electrons of Bi, Sb, Te, Li, C, and O atoms using plane wave-based wave functions was employed [56]. The structure optimization, involving the minimization of ground

state energy, utilized the generalized gradient approximation of Perdew and Wang method that brings the correct exchange-correlation part of electronic energy [57, 58]. A kinetic cutoff energy of 500 eV was set to enhance calculation accuracy. The unit cell of both $\text{Sb}_{0.67}\text{Bi}_{1.33}\text{Te}_3$ and Li_2CO_3 compounds (Figure 1 (B)) extended in all three directions such that the lattice constants become more than 20\AA to sample $1 \times 1 \times 1$ k-meshes of the Brillouin zones, respectively. Ionic and electronic optimizations were alternately performed until the forces on each ion reached less than ± 10 meV/ \AA .

For the $\text{Sb}_{0.67}\text{Bi}_{1.33}\text{Te}_3$ surface interaction (Figure 1 (D)), the Perdew-Burke-Ernzerhof (PBE) functional, within the generalized gradient approximation (GGA), was employed to describe the exchange-correlation energy. A plane-wave basis set was used with an appropriate energy cutoff to ensure energy convergence, and the interaction between valence and core electrons was treated using the projector augmented wave (PAW) method. A cut-off energy was set at 500 eV and the Brillouin zone sampled at gamma point with a k-mesh of $4 \times 4 \times 1$. The convergence criterion of the total energy was set to be within 1×10^{-5} eV within the K-point integration and optimizations were performed until the forces on each atom were below 0.001 eV/ \AA . Finally, to account for the van der Waals interactions, the van der Waals D3 corrections were implemented [59]. Zero-point energy, heat capacity, and entropy corrections were computed using statistical mechanics within the harmonic approximation.

2.2. *Ab initio molecular dynamics (AIMD) and Kubo-Greenwood method for electrical conductivity calculation*

Using optimized structures of $\text{Sb}_{0.67}\text{Bi}_{1.33}\text{Te}_3$ and Li_2CO_3 compounds from our DFT calculation (Figure 1 (B)), we carried out the Ab initio molecular dynamics (AIMD) simulations at 300K up to 1ps with NVT ensemble and 1fs time step to select 10 different frames in the 1ps trajectory data. Subsequently, we generated wavefunctions ($\Psi_{i,k}$ where i and k are band and k-point indices, respectively) data for the selected frames using DFT calculations as explained by Knyazev et. al. [60, 48] to compute the electronic conductivity based on Kubo-Greenwood (KG) formula. During the calculation of wavefunction data from VASP, we included 100% more unoccupied bands than occupied bands for both $\text{Sb}_{0.67}\text{Bi}_{1.33}\text{Te}_3$ and Li_2CO_3 compounds to account for excited state wavefunctions and their corresponding energies. The dynamic electrical conductivity $\kappa(\omega) = \kappa_1(\omega) + i\kappa_2(\omega)$ is represented as a coefficient of the current density $\mathbf{J}(\omega)$ and electric field $\mathbf{E}(\omega)$:

$$\mathbf{J}(\omega) = [\kappa_1(\omega) + i\kappa_2(\omega)]\mathbf{E}(\omega) \quad (1)$$

where ω is the frequency of the external electric field $\mathbf{E}(\omega)$. The important component $\kappa_1(\omega)$ relates to the energy absorbed by the electrons and is computed

by the Kubo-Greenwood formula as [48, 49, 50]

$$\kappa_1(\omega) = \frac{2\pi e^2 \hbar^2}{3m\omega\Omega} \sum_{i,j,\alpha,k} W(k) |\langle \Psi_{i,k} | \nabla_\alpha | \Psi_{j,k} \rangle|^2 [f(\epsilon_{i,k}) - f(\epsilon_{j,k})] \delta(\epsilon_{j,k} - \epsilon_{i,k} - \hbar\omega) \quad (2)$$

Here, the sum is over all \mathbf{k} points in the Brillouin zone, band indices i and j and three spatial dimensions α . $\kappa_1(\omega)$ is the frequency-dependent electrical conductivity. e is the elementary charge. \hbar is the reduced Planck constant. m is the electron mass. ω is the angular frequency. Ω is the volume of the system. f_i and f_j are the Fermi-Dirac distribution functions for states i and j . $|\psi_i\rangle$ and $|\psi_j\rangle$ are the wavefunctions of states i and j . $\epsilon_{i,k}$ and $\epsilon_{j,k}$ are the energies of states i and j . δ is the Dirac delta function. $W(k)$ denotes a weight function at a particular \mathbf{k} point. The wave function $\Psi_{i,\mathbf{k}}$ is generated from our AIMD simulations at room temperature as explained above. $f(\epsilon_{i,\mathbf{k}})$ is the Fermi function. In practical calculations, δ -function is written in terms of the Gaussian function:

$$\delta(\epsilon_{j,k} - \epsilon_{i,k} - \hbar\omega) \rightarrow \frac{1}{\sqrt{2\pi}\Delta E} \exp\left(-\frac{(\epsilon_{j,k} - \epsilon_{i,k})^2}{2(\Delta E)^2}\right) \quad (3)$$

where ΔE is broadening of the δ -function. This technical parameter plays an essential role in controlling the algorithm in the Kubo-Greenwood formula, particularly at low frequencies.

2.3. Atomistic Molecular Dynamics simulations (MD)

Classical Molecular Dynamics (MD) simulations were carried out using the Large-scale Atomic/Molecular Massively Parallel Simulator LAMMPS [61]. A cut-off distance of $r_{cut} = 14 \text{ \AA}$ is used for both Lennard Jones and Coulomb interactions, and a time-step of $\delta t = 1 \text{ fs}$ is utilized. Using a particle-particle particle-mesh solver (PPPM), long-range electrostatic interactions are resolved with an accuracy of 10^{-4} by mapping atomic charges to a 3D mesh, solving Poisson's equation on the mesh via 3D Fast Fourier Transforms (FFTs), and interpolating electric fields from mesh points back to atoms. [62, 63]. The electrolyte is prepared using an DMSO:(EMIM⁺, BF₄⁻) ratio of 3:2, 1M (Li⁺, TFSI⁻), and includes 6000 DMSO molecules, 1857 (EMIM⁺, BF₄⁻) pairs, 566 (Li⁺, TFSI⁻), 14 ZnI₂ and 14 CO₂ molecules, giving a total number of atoms of 113142. Each molecule geometry was optimized using the Generalized Amber Force Field (GAFF) [64] and the Universal Force Field force fields (UFF) [65], successively. Then the Automated force field Topology Builder (ATB) is used to obtain the final GROMOS FF parameters for TFSI⁻, DMSO, EMIM⁺, BF₄⁻, and CO₂ [66, 67, 68]. We note that the ATB parameter generation considers the following: Lennard-Jones parameters refined against experimental solvation and pure liquid properties, ATB parametrization and validation using a single-range 14 \AA cutoff for both Lennard-Jones and Coulomb interactions, atomic charges fitted to quantum mechanical (QM) electrostatic potentials and bonded parameters are assigned using force constants estimated at B3LYP/6-31G* level

of theory, resulting in robust symmetry routines for assigning identical parameters to chemically equivalent atoms, bonds, and angles. For a comprehensive understanding of the ATB parameter generation process, refer to the detailed explanations provided in the original research papers [66, 67, 68]. The UFF interaction potential is used for ZnI_2 . For the Li^+ , the interaction potential parameters were taken from the Canongia Lopes & Padua (CL&P) force field for ionic liquids [69, 70]. The initial distribution was generated using the Moltemplate package [71]. In this process, the simulated system constituents are placed randomly into an oversized cubic box. Then, the system was energetically minimized to ensure optimal particle distribution. The energy minimization algorithm consists of adjusting particle coordinates iteratively [72]. A finite, unitless stopping tolerance for energy ($E_{\text{stop}}=10^{-7}$) that represents the energy variation between consecutive iterations divided by the energy magnitude, and a stopping tolerance for force ($F_{\text{stop}}=10^{-8}$ kcal/Å), are chosen. After that, the system is agitated using the Langevin thermostat [73] at $T=900$ K for $t=1$ ns, followed by the same process using the Nosé-Hoover thermostat [61, 73]. Then, to reach the desired ambient condition of temperature and pressure ($T=300$ K, $P=1$ bar), the simulated systems were equilibrated in the NPT statistical ensemble with isotropic constant pressure control using Berendsen barostat [61, 74]. Firstly, from $T=900$ K to $T=300$ K at a constant pressure of $P=500$ bar for $t=3$ ns. Secondly, the pressure decreases from $P=500$ bar to $P=1$ bar at a constant temperature of $T=300$ K over a time period of $t=3$ ns. In the final NPT equilibration stage, the systems were equilibrated at room temperature and ambient pressure ($T=300$ K, $P=1$ bar) for $t=10$ ns. To investigate the transport properties under conditions similar to experimental settings, we performed simulations in the NVT (constant number of particles, volume, and temperature) statistical ensemble. We employed the Nosé-Hoover thermostat to maintain a constant temperature of 300 K while keeping the volume fixed.

2.4. Finite element model

A mathematical framework has been developed for modeling the behavior of prismatic Li- CO_2 batteries, drawing inspiration from previous studies on Li- O_2 and Li-ion batteries [75, 76, 77]. The model integrates key principles such as mass and current conservation, species transport phenomena, and reaction kinetics within the cathode and separator regions, with the aim of providing deeper insights into the complex mechanisms that occur within the cell during operation. The Li- CO_2 cell under investigation consists of several components: a lithium metal sheet serving as the negative electrode, a separator, a porous carbon cathode coated with $\text{Sb}_{0.67}\text{Bi}_{1.33}\text{Te}_3$, and an organic electrolyte that permeates the porous structures, as illustrated schematically in Figure 1 (A). The used electrolyte composition is described in section 2.3. To facilitate electron transfer, current collectors are located at the rear of both electrodes. This configuration enables a thorough examination of the electrochemical and transport processes that govern battery cell performance and limitations. The main

objective of this mathematical framework is to provide a comprehensive understanding of the intricate interactions among various components and processes within the Li-CO₂ battery cell system.

2.4.1. Electrode Reactions

Cathode Reaction

The main reaction at the cathode is described by [11]:

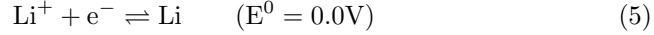


where $E_d^0 = 2.8\text{V}$ and $E_c^0 = 3.8\text{V}$ represent the equilibrium potentials for discharge and charge reactions, respectively [17, 18].

This reaction produces Li₂CO₃/C as the main products during discharge, which plays a crucial role in the battery's performance. Li₂CO₃ and carbon are insoluble in the organic electrolyte and can cover the active surface area inside the porous cathode, block pathways for reactive species (Li⁺ and CO₂), prevent further reactions inside the cathode and thus contribute to the end of cell discharge.

Anode Reaction

The main reaction at the anode, which represents the reversible deposition and dissolution of lithium metal during battery cell operation, is described as [76]:



Where E^0 is the reaction equilibrium potential for charge and discharge [76].

2.4.2. Particle transport at the macroscopic level

The Nernst-Planck equation, a continuity equation for the time-dependent concentration $c_i(t, \mathbf{x})$ of a chemical species, is used to describe the transport of chemical species within the battery cell:

$$\frac{\partial \epsilon c_i}{\partial t} + \nabla \cdot \mathbf{J}_i = r_i \quad (6)$$

In this context, ϵ represents the porosity of the electrode or the electrolyte region in the solution phase, \mathbf{J}_i denotes the flux, and r_i indicates the volumetric production rate of species i transitioning from the electrode material to the electrolyte within the porous structure. The total flux is composed of three components: diffusion, advection, and electromigration. This implies that the concentration is affected by an ionic concentration gradient ∇c , flow velocity \mathbf{v} , and an electric field \mathbf{E} .

$$\mathbf{J} = - \underbrace{D^{eff} \nabla c}_{\text{Diffusion}} + \underbrace{c \mathbf{v}}_{\text{Advection}} + \underbrace{\frac{D^{eff} z e}{k_B T} c \mathbf{E}}_{\text{Electromigration}} \quad (7)$$

In this equation, D^{eff} denotes the effective diffusion coefficient of the chemical species, z represents the valence of the ionic species, e represents the elementary charge, k_B represents the Boltzmann constant, and T represents the absolute temperature. The electric field may be further decomposed as:

$$\mathbf{E} = -\nabla\phi - \frac{\partial\mathbf{A}}{\partial t} \quad (8)$$

where ϕ is the electric potential and A is the magnetic vector potential. Therefore, the Nernst–Planck equation is given by:

$$\frac{\partial c}{\partial t} = \nabla \cdot \left[D^{eff} \nabla c - c\mathbf{v} + \frac{D^{eff}ze}{k_B T} c \left(\nabla\phi + \frac{\partial\mathbf{A}}{\partial t} \right) \right] \quad (9)$$

The primary transport mechanisms in batteries, ionic migration due to electric fields and diffusion due to concentration gradients, are accurately described by the Nernst-Planck equation, which excludes time-varying magnetic effects [78]:

$$\frac{\partial c}{\partial t} = \nabla \cdot \left[D^{eff} \nabla c - c\mathbf{v} + \frac{D^{eff}ze}{k_B T} c \nabla\phi \right] \quad (10)$$

The moving boundaries theory of transference number (t_+) gives [79]:

$$t_+ = \frac{vc_+F}{I\Delta t} \quad (11)$$

where v is the volume occupied by diffusing cations by the boundary in time Δt , c_+ the Li^+ concentration, F the Faraday constant, and I the electric current. By introducing the electrode surface S

$$t_+ = \frac{vc_+F/S}{I\Delta t/S} \quad (12)$$

Also, we can write c as:

$$c = \frac{N}{N_A v} \quad (13)$$

with N the number of particles and N_A the Avogadro number.

Then:

$$t_+ = \frac{\mathbf{J}F}{\mathbf{i}_2} \quad (14)$$

with, \mathbf{J} the molar flux of cations, $i_2 = I/S$ the current density in the electrolyte, and F the Faraday constant.

The primary interest in battery modeling is electrochemical processes rather than fluid dynamics, so the advection term is considered less critical [80]. Furthermore, the porous structure limits large-scale fluid motion, further reducing the importance of advection. By neglecting the Advection term, the Nernst–Planck equation for Li^+ and CO_2 can be expressed as:

$$\mathbf{J}_{\text{Li}^+} = -D_{\text{Li}^+}^{eff} \nabla c_{\text{Li}^+} + \frac{\mathbf{i}_2 t_+}{F} \quad (15)$$

$$\mathbf{J}_{\text{CO}_2} = -D_{\text{CO}_2}^{eff} \nabla c_{\text{CO}_2} \quad (16)$$

The effective diffusion coefficient of a species i ($i=\text{Li}^+, \text{CO}_2$) was calculated using the Bruggeman equation [41, 42]:

$$D_i^{eff} = \epsilon^{1.5} D_i \quad (17)$$

The $\epsilon^{1.5}$ form, in the Bruggeman relation, emerges from the mathematical treatment of a system of spherical particles dispersed in a continuous medium [81]. This form has been found to provide a reasonable empirical fit approximation for many real porous systems, especially at higher porosities [81, 82]. The diffusion coefficient D_i ($i=\text{Li}^+, \text{CO}_2$) is calculated from our MD simulation.

2.4.3. Equations of battery electrochemical properties

The surface density of the liquid phase \mathbf{i}_2 represents the function of the electrolyte concentration c_{Li} , time t , the ionic conductivity σ^{eff} , the absolute temperature T , the activity coefficient $\frac{\partial \ln f_{\pm}}{\partial \ln c_{Li}}$, the universal gas constant R , the cathode porosity ϵ and electrode solution-phase potential ϕ_2 [75, 76].

$$\mathbf{i}_2 = -\sigma^{eff} \nabla \phi_2 + \left(\frac{2\sigma^{eff} RT}{F} + \frac{2\sigma^{eff} RT}{F} \frac{\partial \ln f_{\pm}}{\partial \ln c_{Li}} \right) (1 - t_+) \nabla \ln c_{Li} \quad (18)$$

$$\sigma^{eff} = \epsilon^{1.5} \sigma \quad (19)$$

The solid phase current density \mathbf{i}_1 is the function of the solid-electrode potential and the electronic conductivity of solid-phase mixture [75, 76],

$$\mathbf{i}_1 = -\kappa_{pos}^{eff} \nabla \phi_1 \quad (20)$$

$$\kappa_{pos}^{eff} = (1 - \epsilon_{l,0})^{1.5} \kappa_{pos} \quad (21)$$

$\epsilon_{l,0}$ denotes the starting porosity of the cathode. It is important to mention that the effect of deposits (Li_2CO_3 and carbon) with low conductivity on κ_{pos} was not taken into account, and it was assumed that κ_{pos} would not change even as the battery reactions occurred.

Conservation of charge

$$\nabla \mathbf{i}_1 + \nabla \mathbf{i}_2 = 0 \quad (22)$$

$$\sum_i s_i M_i^{z_i} \rightarrow n e^- \quad (23)$$

$$\nabla \cdot \mathbf{i}_2 = a j \quad (24)$$

These equations demonstrate that the transfer current per unit electrode volume corresponds to the electrode chemical reaction rate, where M_i is a symbol representing a species participating in the electrochemical reaction, z_i and s_i are the charge number and the stoichiometric coefficient of species i , respectively, n is the number of electrons transferred in the reaction, a is the specific interfacial area of the pore per unit electrode volume, and j is the average transfer current.

In the present work, only one electrochemical reaction is considered: the formation of $\text{Li}_2\text{CO}_3/\text{carbon}$ ($\text{Li}_2\text{CO}_3/\text{C}$) inside the porous cathode. In practical cells, battery side reactions can occur during cycling alongside the main electrode reactions. This is reflected by the superficial production rate r_i of a species from the cathode's solid phase to the pore solution, given by Faraday's law as a function of the local transfer current density j_c between the cathode/electrolyte interface.

$$r_i = -\frac{as_i}{nF}j_c \quad (25)$$

Rate expressions

the Butler-Volmer equation is applied in the model using two rate coefficients because the reactions depends on both concentration of Li^+ and CO_2 and concentration of $\text{Li}_2\text{CO}_3/\text{C}$:

$$\frac{j_c}{nF} = k_a(c_{\text{Li}_2\text{CO}_3/\text{C},s}) \exp\left[\frac{(1-\beta)nF}{RT}\eta_c\right] - k_c(c_{\text{Li}^+,s})^2(c_{\text{CO}_2,s}) \exp\left[\frac{-\beta nF}{RT}\eta_c\right] \quad (26)$$

$$\eta_c = \phi_1 - \phi_2 - \Delta\phi_{film} - E^0 \quad (27)$$

$$\phi_{film} = j_c R_{film} \epsilon_s \quad (28)$$

where j_c is local transfer current density between electrode and electrolyte interface, $c_{i,s}$ is the molar concentration of species i at the cathode surface, k_a and k_c are the anodic and cathodic rate constant, respectively, β is a symmetry factor equal to 0.5, η_c is surface or activated overpotential for reaction at cathode, ϕ_{film} and R_{film} are the voltage drop and the electrical resistivity across $\text{Li}_2\text{CO}_3/\text{C}$ film formation, respectively, ϵ_s is the volume fraction of solid $\text{Li}_2\text{CO}_3/\text{C}$, and E^0 is the theoretical open-circuit potential for reaction.

The properties of the $\text{Li}_2\text{CO}_3/\text{C}$ film, specifically its electrical resistivity R_{film} , thickness (Δs), and conductivity (σ_{film}), are related by the equations below:

$$R_{film} = \frac{\Delta s}{\sigma_{film}} \quad (29)$$

$$\Delta s = \Delta s_C + \Delta s_{\text{Li}_2\text{CO}_3/\text{C}} \quad (30)$$

$$\Delta s_i = \frac{\Delta\epsilon_i}{a} = \frac{M_i c_i}{a\rho_i} \quad (31)$$

where i represents Li_2CO_3 or C , while Δs_i , $\Delta\epsilon_i$, M_i , a , and ρ_i refer to the film thickness of i , the change in porosity of the cathode caused by i , the molar mass of i , the specific area, and the density of i , respectively.

The electrochemical reaction at the lithium metal anode, it is given by the general Butler-Volmer equation as follow [75, 76]:

$$j_a = i_0 \exp\left[\frac{(1-\beta)nF}{RT}\eta_a\right] - \exp\left[\frac{-\beta nF}{RT}\eta_a\right] \quad (32)$$

where i_0 is exchange current density for anode, η_a is surface or activated overpotential for reaction at anode, and the other parameter are as described above.

The specific area a of the electrode/electrolyte interface in Equation 31 is decreased by the morphology and dynamic change in porosity due to $\text{Li}_2\text{CO}_3/\text{C}$ solid passivation during electrochemical reaction. This effective local surface area per unit volume of electrode can be commonly written by a geometric relation [75, 76]:

$$a = a_0 \exp \left[1 - \frac{\epsilon_{\text{Li}_2\text{CO}_3/\text{C}}}{\epsilon_{l,0}} \right] \quad (33)$$

where a_0 the initial specific surface area, $\epsilon_{\text{Li}_2\text{CO}_3/\text{C}}$ and $\epsilon_{l,0}$ are the volume fraction of solid $\text{Li}_2\text{CO}_3/\text{C}$ and initial electrode porosity, respectively.

Transport through $\text{Li}_2\text{CO}_3/\text{C}$ layer

During discharge, the formed $\text{Li}_2\text{CO}_3/\text{C}$ creates an additional barrier for Li^+ and CO_2 diffusion from the porous medium to the cathode surface.

This process follows Fick's law [76], where the flux is proportional to the concentration gradient between the bulk electrolyte and the active surface, sustained by ongoing electrochemical reactions consuming reactants.

$$-\frac{as_i}{nF}j_c = \frac{aD_{i,\text{film}}^{\text{eff}}(c_i - c_{i,s})}{l} \quad (34)$$

where $D_{i,\text{film}}^{\text{eff}}$ is the effective diffusion coefficient of species i across the $\text{Li}_2\text{CO}_3/\text{C}$ film, and l is the thickness of the film. c_i represents the molar concentration of species i in the electrolyte, while $c_{i,s}$ denotes the molar concentration of species i specifically at the cathode surface. The effective diffusivity for both Li^+ and CO_2 reactants is used to describe how the pores are deposited by the $\text{Li}_2\text{CO}_3/\text{C}$ formation; this can be described by the Bruggeman relation [41, 42]:

$$-\frac{\partial \epsilon}{\partial t} = \frac{aj_c M_{\text{Li}_2\text{CO}_3/\text{C}}}{2F \rho_{\text{Li}_2\text{CO}_3/\text{C}}} \quad (35)$$

The volume fraction of the solid $\text{Li}_2\text{CO}_3/\text{C}$ and the thickness of the film (l) can be determined from the cathode volume balance as:

$$\epsilon_{\text{Li}_2\text{CO}_3/\text{C}} = 1 - \epsilon - \epsilon_{l,0} \quad (36)$$

$$l = \left[\frac{\epsilon_{\text{Li}_2\text{CO}_3/\text{C}} + \epsilon_{s,0}}{\epsilon_{s,0}} \right]^{(1/3)} r_0 - r_0 \quad (37)$$

In this context, $M_{\text{Li}_2\text{CO}_3/\text{C}}$ and $\rho_{\text{Li}_2\text{CO}_3/\text{C}}$ represent the molar mass and density of $\text{Li}_2\text{CO}_3/\text{C}$, respectively. The term $\epsilon_{s,0}$ denotes the volume fraction of the initial solid phase of the cathode material, while r_0 indicates the radius of the particles within the electrode.

Initial conditions/Boundary conditions

The governing equations consist of partial differential equations that include time and space as independent variables. The dependent variables were simulated using COMSOL Multiphysics 6 finite element analysis software to examine their spatial and temporal changes. The battery cell was segmented into three regions: the anode, separator, and porous cathode. An extra fine mesh was selected for enhanced accuracy. To reduce computation time, a variable-step solver was employed with a relative tolerance of 1×10^{-4} . This solver decreases the total number of time steps required for calculation. The parameters used in the simulations are presented in Tables S1, S2, and S3. The applied current density, i_{app} , was considered positive when directed from the cathode to the external circuit (Figure 1 (A)). The total current density passing through boundary 3 was designated as i_{app} . The Li^+ flux at boundaries 1 and 3 (J_{Li}) and CO_2 flux at boundary 2 (J_{CO_2}) were set to zero. Additionally, the boundary condition $\nabla c_i = 0$ was applied to the relevant boundaries (see Table S2). The parameter c_{CO_2} was assumed to be equal to the saturation concentration, $c_{CO_2,0}$, at boundary 3. The boundary conditions are outlined in Table S2. Discharge simulations were conducted with applied current densities (i_{app}) ranging from 0.1 to 1 mA/cm², defined as positive in the direction from the cathode to the external circuit.

3. Results and discussion

3.1. Electrical conductivity from DFT, AIMD and Kubo-Greenwood formula

Calculated dynamic electrical conductivities for both $\text{Sb}_{0.67}\text{Bi}_{1.33}\text{Te}_3$ and Li_2CO_3 are shown in Figure 2, for decremented values of ΔE from 0.9 to 0.54 with a step of 0.04. The electrical conductivities calculated for different values of ΔE show the conductive behavior of $\text{Sb}_{0.67}\text{Bi}_{1.33}\text{Te}_3$ (a conductivity range of the order of 10^5 S/m) and insulative behavior of Li_2CO_3 (a conductivity range of the order of 10^{-3} S/m). Quantitatively, the electrical conductivities converge with decreasing ΔE , i.e., the dependence of conductivity on ΔE is smaller. The static electrical conductivities at zero frequency are calculated by interpolating small frequency data shown in Figure 2 (a2) and (b2). Using ΔE values where conductivity is converged, below 0.66 for $\text{Sb}_{0.67}\text{Bi}_{1.33}\text{Te}_3$ and below 0.86 for Li_2CO_3 , our computational analysis reveals a static electrical conductivity of $(1.43 \pm 0.3) \times 10^5$ S/m for $\text{Sb}_{0.67}\text{Bi}_{1.33}\text{Te}_3$, indicating its strong electrical conducting properties. This finding aligns with the well-established characteristics of bismuth telluride (Bi_2Te_3) and its alloys, which are extensively employed in thermoelectric devices due to their good electrical conductivity [83, 84]. The high conductivity can be ascribed to the semiconductor nature of Bi_2Te_3 and the antimony (Sb) doping effect, which augments the carrier concentration [85]. Experimental investigations on Bi_2Te_3 have reported electrical conductivity values as high as 1.22×10^5 S/m [84], further corroborating the computational results.

Our calculations reveal that lithium carbonate (Li_2CO_3) exhibits a static electrical conductivity range of $0.1 - 2 \times 10^{-3}$ S/m, indicating its poor electrical conductivity and insulating behavior [86]. This calculated value aligns closely with experimentally reported values, 2×10^{-3} S/m [87] and 3.16×10^{-4} S/m [88]. The insulating nature of Li_2CO_3 can be attributed to its ionic nature and the strong ionic bonds that hinder electron mobility [89].

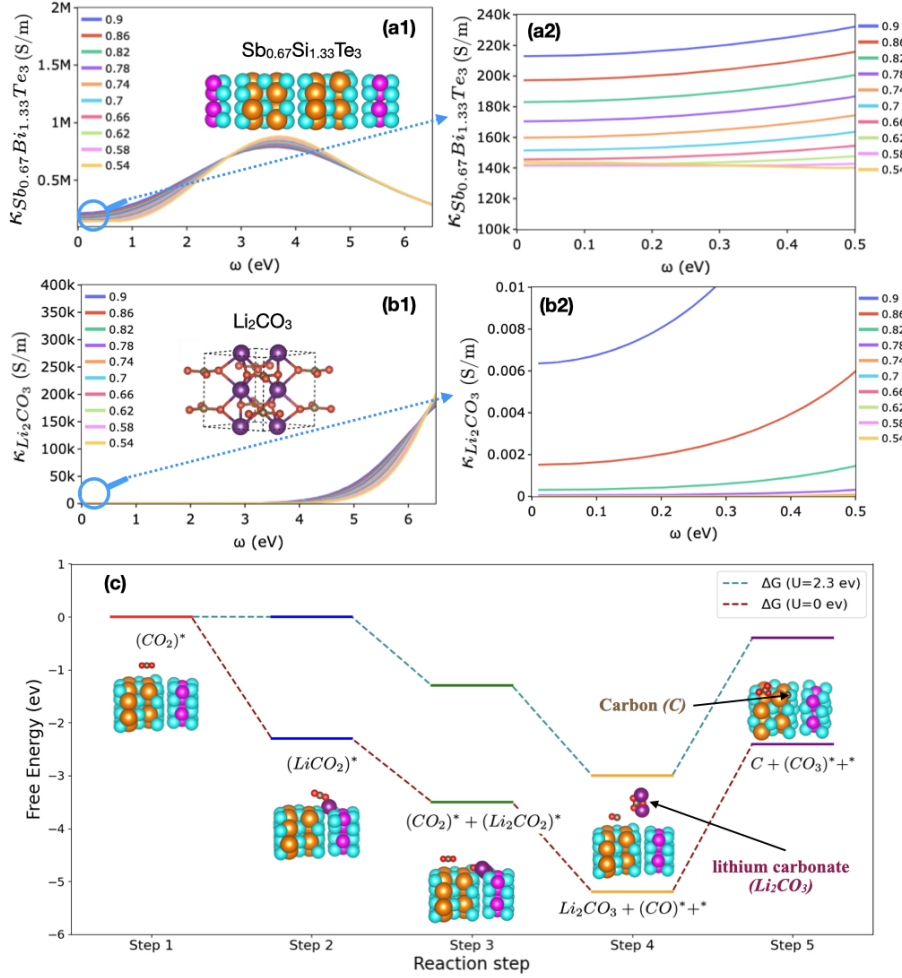


Figure 2: Dynamic electrical conductivity of (a1-a2) $\text{Sb}_{0.67}\text{Bi}_{1.33}\text{Te}_3$ and (b1-b2) Li_2CO_3 calculated using the Kubo-Greenwood formula for (a1 and b1) a wide frequency range and (a2 and b2) a small frequency range. The electrical conductivity is plotted using ΔE values decremented from 0.9 to 0.54 with a step of 0.04. (c) Free energy landscape of the CO_2 reduction reaction leading to the formation of $\text{Li}_2\text{CO}_3/\text{C}$ deposits on the $\text{Sb}_{0.67}\text{Bi}_{1.33}\text{Te}_3$ surface, with inset images illustrating the optimized geometries of key reaction intermediates.

Calculated dynamic electrical conductivities for both $\text{Sb}_{0.67}\text{Bi}_{1.33}\text{Te}_3$ and

Li₂CO₃ are shown in Figure 2 (a1) and (b1) for a large frequency range and in Figures 2 (a2) and (b2) for a small frequency range, for decremented values of ΔE from 0.9 to 0.54 with a step of 0.04. Figures 2 (a2) and (b2), the electrical conductivities converge, for small frequencies, with decreasing ΔE , i.e., the dependence of conductivity on ΔE becomes smaller. The static electrical conductivities at zero frequency are calculated by interpolating small frequency data shown in Figures 2 (a2) and (b2), using ΔE values where conductivity has converged, below 0.66 for Sb_{0.67}Bi_{1.33}Te₃ and below 0.86 for Li₂CO₃. The static electrical conductivities calculated for different values of ΔE show the conductive behavior of Sb_{0.67}Bi_{1.33}Te₃ (a conductivity range on the order of 10⁵ S/m) and insulative behavior of Li₂CO₃ (a conductivity range on the order of 10⁻⁴-10⁻³ S/m). Our computational analysis reveals a static electrical conductivity of $(1.43 \pm 0.3) \times 10^5$ S/m for Sb_{0.67}Bi_{1.33}Te₃, indicating its strong electrical conducting properties. This finding aligns with the well-established characteristics of bismuth telluride (Bi₂Te₃) and its alloys, which are extensively employed in thermoelectric devices due to their good electrical conductivity [83, 84]. The high conductivity can be attributed to the semiconductor nature of Bi₂Te₃ and the antimony (Sb) doping effect, which augments the carrier concentration [85]. Experimental investigations on Bi₂Te₃ have reported electrical conductivity values as high as 1.22×10^5 S/m [84], further corroborating the computational results. Our calculations reveal that lithium carbonate (Li₂CO₃) exhibits a static electrical conductivity range of $0.1 - 2 \times 10^{-3}$ S/m, indicating its poor electrical conductivity and insulating behavior [86]. This calculated value aligns closely with experimentally reported values of 2×10^{-3} S/m [87] and 3.16×10^{-4} S/m [88]. The insulating nature of Li₂CO₃ can be attributed to its ionic nature and the strong ionic bonds that hinder electron mobility [89]. In Li₂CO₃, Li⁺ ions act as the primary charge carriers rather than electrons, a characteristic typical of ionic compounds. The low conductivity of Li₂CO₃ presents challenges to battery performance, including high internal resistance and passivation of the electrode surface [90, 91]. To address these challenges, potential solutions include enhancing Li₂CO₃ conductivity, promoting its decomposition through conductive additives or catalysts, designing porous electrodes for increased surface area, and exploring alternative Li₂CO₃ structures with improved conductivity or decomposition properties.

3.2. Surface reaction of Sb_{0.67}Bi_{1.33}Te₃ as cathode catalyst

The DFT calculations of the reaction path for Li₂CO₃/C formation on the Sb_{0.67}Bi_{1.33}Te₃ as Li-CO₂ battery cathode catalyst have revealed intriguing insights into the adsorption behavior of reaction products and the step-wise mechanism of the discharge process. To comprehensively understand the formation of Li₂CO₃/C and C, we calculated the Gibbs free energy (ΔG) changes for various elementary reaction steps on the Sb_{0.67}Bi_{1.33}Te₃ catalyst surface, revealing a sequence of intermediate stages that elucidate the complex reaction pathway.

The Gibbs free energy G of the reaction was calculated using the following

equation:

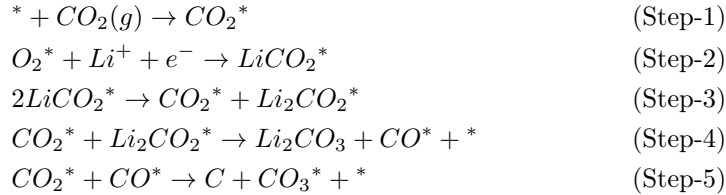
$$G = E + \text{ZPE} + \int_0^T C_p dT - TS \quad (38)$$

where ZPE is the zero-point energy, C_p is the heat capacity, S is the entropy, T is the temperature, and E is the electronic energy.

We considered ZPE and entropy changes in Step-1 and assumed that these changes for other elementary steps are small and therefore negligible. The potential-dependent reaction energies were calculated based on the computational hydrogen electrode (CHE) model with reference to the Li/Li⁺ electrode [92, 93]. The potential-dependent reaction energies profile is shown in Figure 2 (c), and the respective reaction energies of each step are shown in Table 1. To level up the electrochemical step, a potential was applied to the formation of LiCO₂. As can be seen in Figure 2 (c), this potential occurs at 2.3 V versus Li/Li⁺ electrode.

The reaction begins with the adsorption of CO₂* on the Bi site, with a Bi-O distance of 3.5 Å. This initial step is marginally endergonic, with a ΔG of 0.002 eV, indicating a slight energy barrier to CO₂ adsorption. Following this step, the coupled addition of Li⁺ and an electron to the adsorbed CO₂* forms the LiCO₂* intermediate. This step is highly exergonic, with a ΔG of -2.3 eV, suggesting a thermodynamically favorable process that likely drives the overall reaction forward. The reaction pathway continues with the interaction between two LiCO₂* intermediates, producing Li₂CO₂* and CO₂*. This step has a ΔG of -1.2 eV, indicating another energetically favorable process. Subsequently, a pivotal step occurs: the conversion of Li₂CO₂* and CO₂* into Li₂CO₃ and CO*, with a ΔG of -1.7 eV. This step is crucial as it marks the formation of one of the main discharge products, Li₂CO₃. The final step in the pathway involves the generation of carbon, facilitated through the reaction of CO* and CO₂*. Interestingly, this step is energetically uphill, with a ΔG of 2.8 eV, and also produces CO₃* on the surface. This energy barrier for carbon formation could explain the observed preferential adsorption of carbon on the catalyst surface, as the system may need to overcome this energy barrier to complete the carbon formation process.

The complete 5-step reaction pathway can be summarized as follows:



These results highlight the essential role of coupled electron-cation transfer processes in the growth of discharge products. The strong exergonic nature of steps 2-4 suggests that these processes occur readily, while the endergonic nature of the final carbon formation step aligns with the observed preferential adsorption

of carbon on the $\text{Sb}_{0.67}\text{Bi}_{1.33}\text{Te}_3$ catalyst surface. The lack of Li_2CO_3 adsorption on the catalyst surface, as indicated by the simulation, can be explained by the reaction pathway. Li_2CO_3 is formed in step 4, but this step also releases CO^* and a free surface site (*). This suggests that Li_2CO_3 formation occurs near, but not directly on, the catalyst surface, reducing the cathode porosity and possibly clogging the cathode pores.

These insights into the reaction mechanism have significant implications for catalyst design and overall battery performance. The strong affinity of carbon for the catalyst surface, coupled with the energetically unfavorable step of its formation, suggests that catalyst degradation through carbon accumulation could be a concern over long-term battery operation. This highlights the need for strategies to mitigate carbon build-up, such as developing self-cleaning catalysts or implementing periodic regeneration protocols. Furthermore, the spatial separation of Li_2CO_3 formation from the immediate catalyst surface underscores the importance of electrolyte engineering in Li- CO_2 battery design. Since Li_2CO_3 formation appears to occur away from the catalyst, the electrolyte’s ability to facilitate Li_2CO_3 formation, dissolution, and transport becomes crucial. This suggests that future research should focus on developing electrolytes or additives that can enhance Li_2CO_3 solubility or promote its formation and decomposition.

Table 1: Reaction energies of each of the elementary steps.

Reaction Step	Reaction Steps	ΔG (eV)
Step-1	$\Delta G = G(\text{CO}_2^*) - G(*) - G(\text{CO}_{2,gas})$	0.002
Step-2	$\Delta G \approx \Delta E = E(\text{LiCO}_2^*) - E(\text{Li}^+ + e^-) - E(\text{CO}_2^*)$	-2.3
Step-3	$\Delta G \approx \Delta E = E(\text{Li}_2\text{CO}_2^*) + E(\text{CO}_2^*) - 2E(\text{LiCO}_2^*)$	-1.2
Step-4	$\Delta G \approx \Delta E = E(\text{Li}_2\text{CO}_3) + E(*) + E(\text{CO}^*) - E(\text{Li}_2\text{CO}_2^*) - E(\text{CO}_2^*)$	-1.7
Step-5	$\Delta G \approx \Delta E = E(\text{C}) + E(\text{CO}_3^*) + E(*) - E(\text{CO}^*) - E(\text{CO}_2^*)$	2.8

3.3. Li- CO_2 battery electrolyte transport properties and Li^+ solvation structure from large scale MD simulation.

This section presents the results of MD simulations that elucidate the atomic-level dynamic and solvation properties of the Li- CO_2 battery electrolyte depicted in Figure 1 (C). These simulations provide microscopic insights into the electrolyte’s behavior, bridging the gap between atomic and macroscopic transport properties in our multiscale approach.

3.3.1. Li- CO_2 battery electrolyte transport properties

The primary goal is to investigate the electrolyte’s dynamic properties governing ion and CO_2 transport mechanisms, including ionic conductivity, cation transference number, and CO_2 diffusion coefficient, as presented in Table 2.

These properties directly impact the Li-CO₂ battery’s electrochemical performance.

The cations transference number is assessed by [94]:

$$t_+ = \frac{D_{\text{Li}^+}}{D_{\text{Li}^+} + D_{\text{TFSI}^-}} \quad (39)$$

Where the self-diffusion coefficients are determined from the mean-square-displacement of center of mass presented in Figure S1, calculated from the MD simulations as follows [95]:

$$\Delta^2 \mathbf{r}_{CM}(t) = \langle \Delta^2 \mathbf{r}(t) \rangle = \frac{1}{N} \sum_{i=1}^N [\mathbf{r}_i(t+t_0) - \mathbf{r}_i(t_0)]^2 \quad (40)$$

In the expression above, $\mathbf{r}_i(t)$ represents the temporal position of a random walker (ion i or CO₂ molecule). Here, t indicates the time and t_0 is an initial time at which the random walker begins to move. The diffusion coefficients are extrapolated from the normal diffusion regime characterized by:

$$\langle \Delta^2 r \rangle = 6Dt, \quad t > \tau \quad (41)$$

where τ is crossover time to the normal diffusion regime.

The Green-Kubo (GK) approach [52] that takes the autocorrelation with respect to the ionic current in the electrolyte \mathbf{J} is used to calculate the ionic conductivity σ :

$$\sigma = \frac{V}{k_B T} \int_0^\infty dt \langle \mathbf{J}(t) \cdot \mathbf{J}(0) \rangle \quad (42)$$

with,

$$\mathbf{J}(t) = q \sum_i^N z_i \mathbf{v}_i(t) \quad (43)$$

Here q is the elementary charge, z_i represents the charge number (valence) of ion i , \mathbf{v}_i is the velocity of ion i , T is temperature, k_B is the Boltzmann constant, V is the volume of the simulation box, and N is the number of ions.

Table 2: Computed parameters from our MD simulation.

Parameter	Value	Unit	Symbol
Diffusion coefficient of Li ⁺	3.17	10 ⁻⁹ m ² s ⁻¹	D _{Li⁺}
Ionic conductivity	6.77 (7.4) ^a	mS cm ⁻¹	σ
Transference number of Li ⁺	0.91 (0.88) ^a	—	t_+
Diffusion coefficient of CO ₂	1.2 (1.16) ^b (1.14) ^c	10 ⁻⁹ m ² s ⁻¹	D _{CO₂}

^a Results for 1M LiTFSI/DMSO electrolyte [96]

^b SEGWE Equation [97]

^c Einstein equation [97]

The estimated diffusion coefficient of CO₂ in DMSO at 25 °C is approximately 1.16×10^{-9} m²/s using the Stokes-Einstein-Gierer-Wirtz (SEGWE) relation and 1.14×10^{-9} m²/s using the Einstein equation [97]. These values are consistent with our MD calculation result of 1.2×10^{-9} m²/s presented in Table 2, further validating our findings.

3.3.2. Li⁺ solvation structure from large scale MD simulation

The structural analysis was conducted utilizing the Radial Distribution Function (RDF), $g(r)$, and Coordination Number (N_c). The RDF quantifies the spatial distribution of particles relative to a reference particle, providing insights into the local structural organization that affect the transport properties in the electrolyte.

The RDF is mathematically expressed as:

$$g_{\alpha\beta}(r) = \frac{\langle \rho_{\beta}(r) \rangle}{\langle \rho_{\beta} \rangle_{local}} = \frac{1}{\langle \rho_{\beta} \rangle_{local}} \frac{1}{N_{\alpha}} \sum_{i \in \alpha} \sum_{j \in \beta} \frac{\delta(r_{ij} - r)}{4\pi r^2} \quad (44)$$

with $\langle \rho_{\beta}(r) \rangle$ the particle density of type β at a distance r around particles α , and $\langle \rho_{\beta} \rangle_{local}$ the particle density of type β averaged over all spheres around particles α with radius r_{max} . Here, we chose $r_{max}=12\text{\AA}$.

The primary peak in $g(r)$ corresponds to the nearest neighbors, indicating the most probable interparticle distance and interaction strength. This relationship is described by $g(r) = e^{(-\beta U(r))}$, where $\beta = 1/(k_B T)$ and $U(r)$ is the interaction potential. Subsequent peaks in the RDF elucidate higher-order neighbor relationships, offering insights into medium-range order, coordination numbers, and packing efficiency. In isotropic, homogeneous systems, $g(r)$ asymptotically approaches unity at large distances, signifying uniform particle distribution.

The coordination number, N_c, is defined as the number of neighboring particles within a specified cutoff distance of the pair interaction potential from a central particle. It is mathematically represented as:

$$N_c = 2\pi \int_0^{r_c} n_r r dr = 2\pi n_b \int_0^{r_c} g(r) r dr \quad (45)$$

where r_c denotes the distance at which the interparticle interaction potential approaches zero, n_b represents the bulk density, and n_r is the average number density of particles at a given distance r , related to the RDF by $n_r = n_b g(r)$.

The coordination number as a function of distance, N(r), is expressed as:

$$N(r) = 2\pi n_b \int_0^r g(r') r' dr' \quad (46)$$

where r represents an arbitrary distance from a reference particle.

We present the average Radial Distribution Function ($g(r)$) and Coordination Number ($N(r)$) profiles for BF₄⁻, TFSI⁻, and EMIM⁺ ions, as well as DMSO solvent, surrounding a single Li⁺ ion. Additionally, we analyze the $g(r)$

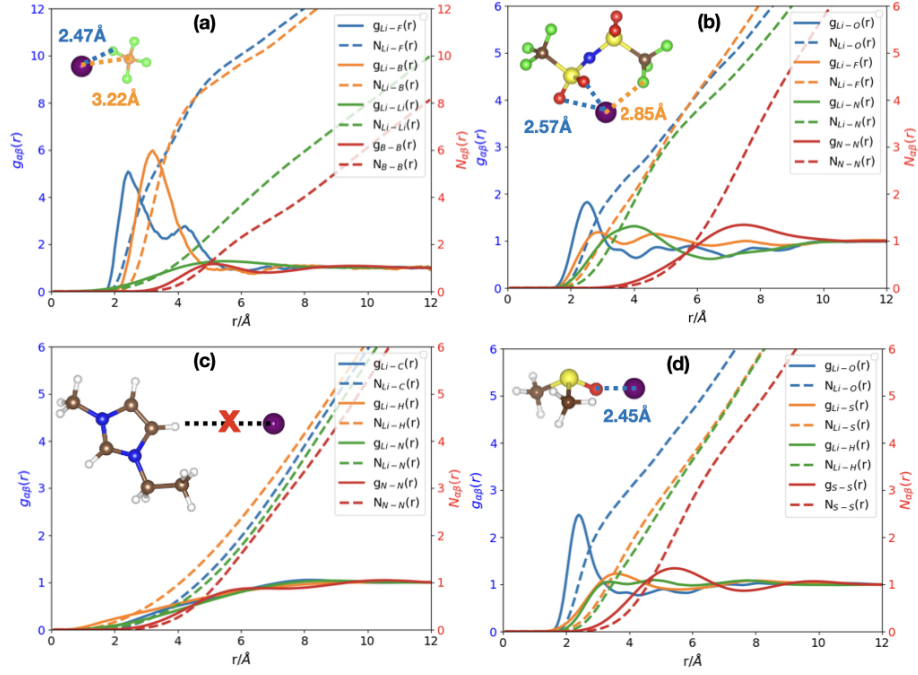


Figure 3: Comparison of the average Radial Distribution Function ($g(r)$) and Coordination Number ($N(r)$) profiles for BF_4^- (a), TFSI^- (b), and EMIM^+ ions (c), as well as DMSO solvent (d), surrounding a single Li^+ ion. Additionally, the $g(r)$ and $N(r)$ between molecules of the same type are represented, which can be referred to as the $g(r)$ and $N(r)$ of the center-of-mass atoms of the molecules.

and $N(r)$ between molecules of the same type, represented by their center-of-mass atoms. Li^+ ions preferentially coordinate with molecules containing highly electronegative atoms, i.e., atoms with a negative partial charge. The flat $g(r)$ curves in Figure 3 (c) indicate a weak interaction between Li^+ and EMIM^+ . Consequently, Li^+ primarily coordinates with BF_4^- , TFSI^- , and DMSO. According to Figure 3 (a), (b), and (d), Li^+ ions interact strongly with BF_4^- , TFSI^- , and DMSO. The most probable distances between Li^+ and the constituent atoms are: BF_4^- ($\text{Li}^+\text{-F} \approx 2.47 \text{ \AA}$, $\text{Li}^+\text{-B} \approx 3.22 \text{ \AA}$), TFSI^- ($\text{Li}^+\text{-O} \approx 2.57 \text{ \AA}$, $\text{Li}^+\text{-F} \approx 2.85 \text{ \AA}$), and DMSO ($\text{Li}^+\text{-O} \approx 2.45 \text{ \AA}$). The Li^+ cations in the electrolyte are more solvated by BF_4^- and DMSO than TFSI^- , as evidenced by the higher peaks in the $g(r)$ and the corresponding coordination number curves of $\text{Li}^+\text{-BF}_4^-$. BF_4^- and DMSO are closer to the Li^+ ions than TFSI^- ions, playing a crucial role in the dissociation of LiTFSI salt. However, TFSI^- can also access the first coordination shell of Li^+ due to strong interactions between its O and F atoms and Li^+ . The presence of both BF_4^- and TFSI^- facilitates favorable coordination between Li^+ and F, potentially leading to the formation of a Li-F solid electrolyte interphase (SEI) that protects the Li-metal anode.

Interactions between molecules of the same type are weak due to electrostatic repulsion, resulting in well-dispersed molecules throughout the simulated electrolyte. The average first shell coordination number values for a tagged Li^+ cation were determined using a threshold distance of 3 Å, based on the range of the first $g(r)$ peaks. Key findings from the coordination number analysis include: Li^+ - Li^+ ($N(r = 3\text{Å}) \approx 0.5$, $N(r = 5\text{Å}) \approx 1$), Li^+ - BF_4^- ($N_{\text{Li-F}}(r = 3\text{Å}) \approx 4.4$, $N_{\text{Li-B}}(r = 3\text{Å}) \approx 2.2$), Li^+ -DMSO ($N_{\text{Li-O}}(r = 3\text{Å}) \approx 2.2$), and Li^+ -TFSI $^-$ ($N_{\text{Li-O}}(r = 3\text{Å}) \approx 1.8$, $N_{\text{Li-F}}(r = 3\text{Å}) \approx 1$, $N_{\text{Li-N}}(r = 3\text{Å}) \approx 0.6$).

The high ionic conductivity and transference number (Table 2) of the simulated electrolyte is derived from several key factors revealed by the solvation structure and interaction analyses Figure 3. Li^+ cations are preferentially solvated by BF_4^- and DMSO, promoting LiTFSI salt dissociation and increasing free charge carriers. Weak Li^+ -TFSI $^-$ interactions facilitate easier Li^+ transport. The presence of BF_4^- and TFSI $^-$ creates Li^+ conducting channels through favorable Li^+ -F coordination. Well-dispersed ionic species due to weak same-type molecular interactions enhance efficient ion transport. Optimal coordination numbers (e.g., $N_{\text{Li-F}}(r = 3\text{Å}) \approx 4.4$ for BF_4^- , $N_{\text{Li-O}}(r = 3\text{Å}) \approx 2.2$ for DMSO) allow efficient Li^+ transport while maintaining sufficient solvation. Low Li^+ - Li^+ coordination ($N(r = 3\text{Å}) \approx 0.5$) minimizes clustering, promoting ion mobility. Multiple solvating species create a dynamic environment, facilitating rapid solvating molecule exchange and enhancing Li^+ mobility. The preferential solvation of Li^+ by BF_4^- and DMSO allows for more free movement compared to the larger TFSI $^-$ anions, resulting in a higher proportion of the ionic current carried by Li^+ and thus increasing the Li^+ transference number.

3.4. Cell performance from finite element analysis

The simulated voltage-capacity curves of the Li- CO_2 battery cell during the charge-discharge phase is presented in Figure 4 (a). This curve was derived from finite element analysis (FEA) using the atomistic simulation results shown in Figure 2 and Table 2, along with other parameters detailed in Tables S1, S2, and S3. The FEA results were compared with the experimental data obtained from the set-up described in the Supporting Information (SI), at a current density of 1 mA/cm 2 . The data illustrated in Figure 4 (a) indicate a strong correlation between the simulated results and the experimental voltage. During discharge, the cell potential exhibited a rapid decline from 3.1 V to a plateau of approximately 2.65 V, followed by a gradual reduction to the cutoff voltage of 2.2 V. During charging, the cell potential increased rapidly from 3.7 V to a plateau of 4.2 V, followed by a gradual rise to the cutoff voltage of 4.5 V. Furthermore, the specific capacity, calculated on the basis of the catalyst mass, was about 6200 mAh/g (2.48 mAh/cm 2).

Figure 4 (b) illustrates the impact of applied current density on the simulated discharge curves of Li- CO_2 battery cell. The discharge capacity exhibits a substantial reduction, decreasing from 81,570 mAh/g at a low current density of 0.1 mA/cm 2 to 6,200 mAh/g at a higher current density of 1 mA/cm 2 . This

observation aligns with prior experimental results, indicating that current density has a significant influence on cell capacity [98]. Furthermore, the discharge voltage plateau decreases as the current density increases (Figure 4 (b)). The capacity decrease at elevated discharge rates can be attributed to limitations in CO_2 transport through the cathode, which becomes saturated with electrolyte and unable to sustain the electrochemical reaction. Consequently, as the discharge rate escalates, CO_2 reduction is confined to a localized area near the cathode-current collector interface. Furthermore, the rapid reduction in porosity due to Li_2CO_3 and C deposition on the active area's surface further impedes CO_2 transport into the cell, preventing complete utilization of the electrode's porosity. Figures 5, S3 and S4 illustrate and analyze these phenomena in detail. Figure S2 illustrates the overpotential behavior of the studied Li- CO_2 battery

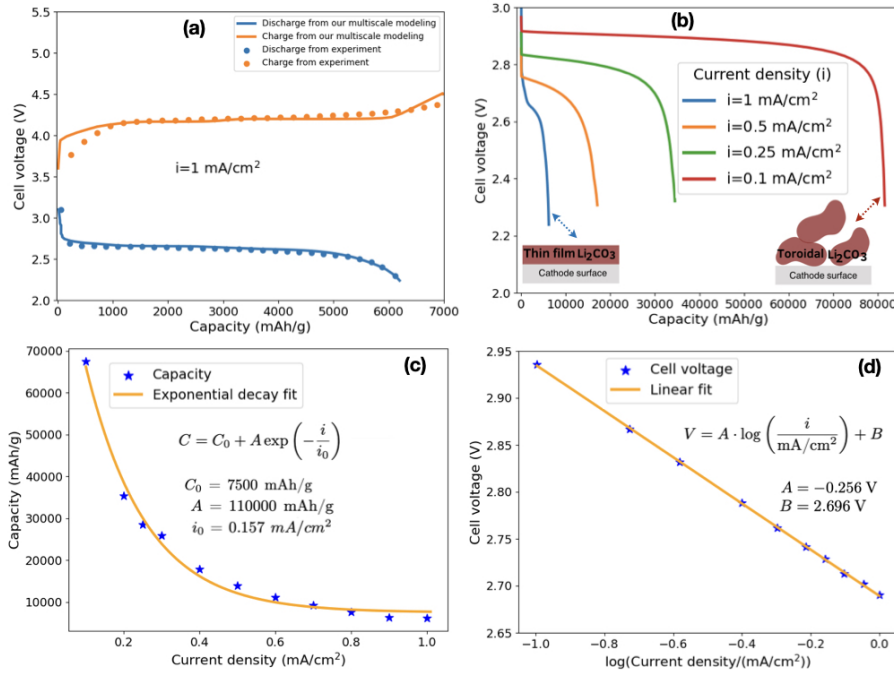


Figure 4: (a) Deep discharge/charge curve of the Li- CO_2 battery cell operating at 1 mA/cm^2 obtained from our multiscale model and experiment. (b) Deep discharge curves of Li- CO_2 battery cell operating at different applied current densities of 1 mA/cm^2 , 0.5 mA/cm^2 , 0.25 mA/cm^2 and 0.1 mA/cm^2 . (c) capacity as a function of discharge current density. (d) Cell potential at the start of discharge voltage plateau with respect to current density. The cathode has a thickness of 2 mm and an initial porosity of 0.73 and other parameters are used as presented in Tables S1, S2, and S3.

cell during discharge, revealing a transition from a positive overpotential to a negative overpotential. The initial positive overpotential can be attributed to kinetic and mass transport limitations associated with the CO_2 reduction reac-

tion (ORR) at the cathode. This phenomenon is consistent with observations in other battery systems, such as vanadium-manganese flow batteries, where kinetic barriers result in a positive overpotential during discharge [99]. As the discharge progresses, the overpotential becomes negative, indicating a shift in the reaction dynamics. This transition is due to morphological changes in the cathode surface or discharge products (Figure 5 (a1) and (a2)) that could create a more favorable electrochemical environment [22]. Furthermore, as the discharge continues, the distribution of reactants and products becomes more balanced, alleviating initial transport limitations. This phenomenon is related to the morphological changes observed in the cathode surface during discharge (Figure 5 (a1) and (a2)). We note that Li *et al.* reported that the formation of $\text{Li}_2\text{C}_2\text{O}_4$ (lithium oxalate) particles on the cathode surface created a more favorable electrochemical environment by providing additional active sites, improving conductivity and increasing the effective surface area [100]. These changes resulted in higher discharge capacity and improved cycling stability, underscoring the complexity of the discharge process and the importance of optimizing materials and design to enhance overall battery cell performance.

The observed behavior where the overpotential in the Li- CO_2 battery cell during discharge decreases to 0 V as current density increases from 0.1 to 1 mA/cm^2 can be explained by changes in the morphology and formation mechanism of $\text{Li}_2\text{CO}_3/\text{C}$ (Figure 5 (a1) and (a2)). It has been found for the Li-air battery that at lower current densities, the deposited species (Li_2O_2) tends to form larger, toroidal structures, which can lead to higher overpotentials due to less efficient electron transport [101, 102, 103]. Similarly to what was observed for Li- O_2 battery, as the current density increases in Li- CO_2 battery, the deposited species, Li_2CO_3 and carbon form a thin film (see Figure 5 (a1) and (a2)), which maintains closer contact with the surface of the conductive catalyst, thus reducing the overpotential (Figure S2) because Li_2CO_3 has low electrical conductivity (Figure 2). Figure 4 (c) shows that the capacity of the studied Li- CO_2 battery cell decreases exponentially with increasing current density, as can be described by the following equation [102]:

$$C = C_0 + A \exp\left(-\frac{i}{i_0}\right) \quad (47)$$

where: $C_0 = 7500 \text{ mAh/g}$ is the baseline capacity, $A = 110000 \text{ mAh/g}$ is a scaling factor, $i_0 = 0.157 \text{ mA}/\text{cm}^2$ is a characteristic current density. At low current density ($i \ll 0.157 \text{ mA}/\text{cm}^2$), the capacity C tends towards its maximum value of 117500 mAh/g . This is the sum of the baseline capacity (C_0) and the additional capacity represented by A . As the current density i increases, there is a rapid decrease in the additional capacity provided by A , resulting in a decrease in the total capacity C . The parameter i_0 determines the rate at which the capacity decreases with increasing current density. A smaller i_0 would mean a faster decrease in capacity for a given increase in current density, while a larger i_0 would indicate a slower decrease. As the current density increases further, the

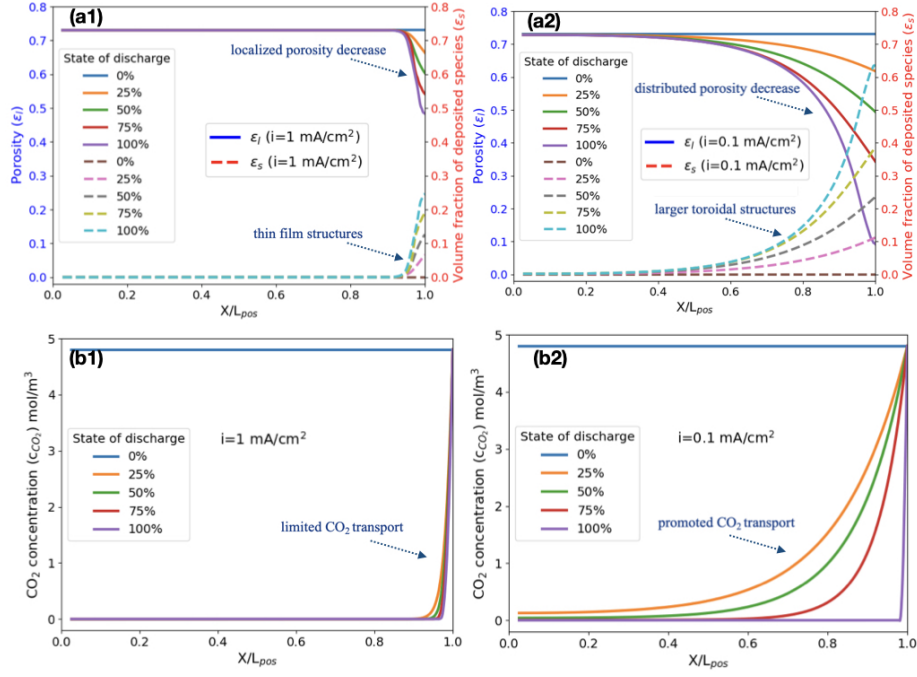


Figure 5: The changes in porosity and volume fraction of deposited species throughout the discharge process are shown at different current densities ((a1) 1 mA/cm^2 and (a2) 0.1 mA/cm^2) in relation to the state of discharge. The local CO_2 concentration within the Li- CO_2 cathode during discharge was analyzed at rates of 0.1 mA/cm^2 (b1) and 1 mA/cm^2 (b2), corresponding to different discharge levels (0% indicates a fully charged battery). The distance (X) is normalized by the cathode length (L_{pos}), where $X/L_{pos}=0$ corresponds to the cathode/separator interface and $X/L_{pos}=1$ corresponds to the cathode/current collector interface.

capacity approaches the baseline value C_0 of 7500 mAh/g . This suggests that at high current densities, the battery's capacity is primarily limited to its baseline capacity, as the contribution from the exponential term becomes negligible. The exponential decrease in capacity with increasing current density highlights a trade-off between power output and energy capacity [104]. At higher current densities ($i \gg 0.157 \text{ mA/cm}^2$), the battery can deliver more power, but at the cost of reduced capacity. This is a critical consideration in applications where both high-power and high-capacity are required. The connection between cell voltage (V) and current density (i) during the discharge of the studied Li- CO_2 battery cell in Figure 4 (d) is represented by the formula [102, 105]:

$$V = A \cdot \log \left(\frac{i}{\text{mA/cm}^2} \right) + B \quad (48)$$

where $A = -0.256 \text{ V}$ and $B = 2.696 \text{ V}$. The parameter A represents the slope of the voltage change with the logarithm of the current density (mAcm^{-2}), while B

represents the voltage at a reference current density of 1 mA/cm^2 . This formula indicates that as the current density increases, the cell voltage decreases logarithmically, a common characteristic in electrochemical cells due to increased polarization and decreased voltage at higher current densities [102, 105].

Figure 5 (a1) and (a2) illustrate how porosity (ϵ_l) and volume fraction of $\text{Li}_2\text{CO}_3/\text{C}$ deposited species (ϵ_s) change over space and time with current densities of $i=1 \text{ mA/cm}^2$ and $i=0.1 \text{ mA/cm}^2$, respectively. Figure S3 presents a comparison of these parameters at $i=0.1, i=0.25, i=0.5,$ and $i=1 \text{ mA/cm}^2$. For high current density ($i=1 \text{ mA/cm}^2$), porosity decreases gradually, primarily near the CO_2 feed side of the cathode ($X/L_{pos}=1$), from its initial value of $\epsilon_l = 0.73$ to 0.48 at the end of discharge. This decrease is due to the formation of a thin film of $\text{Li}_2\text{CO}_3/\text{C}$, represented by the gradual increase of ϵ_s from 0 to 0.25 near the cathode feed side. This film formation leads to electrode clogging, impeding efficient CO_2 diffusion into the cathode. For low current density ($i=0.1 \text{ mA/cm}^2$), $\text{Li}_2\text{CO}_3/\text{C}$ forms larger toroidal structures [101, 102, 103], evidenced by the gradual increase of ϵ_s across a wider region of the cathode from 0 to 0.64. This results in a distributed porosity decrease from 0.73 to 0.09, initially allowing more CO_2 transport into the cathode. However, as discharge progresses, the substantial porosity decrease hinders CO_2 diffusion even at low current densities. Figure 5 (b1) and (b2) present the CO_2 concentration profiles within the cell during discharge at $i=1 \text{ mA/cm}^2$ and $i=0.1 \text{ mA/cm}^2$, respectively. Figure S4 compares concentration profiles at various current densities. At $i=1 \text{ mA/cm}^2$, the CO_2 concentration (c_{CO_2}) decreases sharply from its initial value of 4.8 mol/m^3 to 0 mol/m^3 in the porous cathode, indicating strongly impeded CO_2 diffusion. At $i=0.1 \text{ mA/cm}^2$, the decrease is more gradual. The impediment to CO_2 transport, which is inversely proportional to the current density, results from the accumulation of Li_2CO_3 and carbon on the active cathode surface. This accumulation reduces pore availability for the electrolyte, increases the amount of insulating species, and obstructs pores, collectively restricting CO_2 transport and limiting cell capacity (Figure 4 (c)). To address these limitations, an ideal cathode should feature: large surface area for reaction sites and product deposition, large pores to facilitate active species transport and prevent clogging, high porosity to accommodate discharge product growth, and high electrical conductivity and stability. Such a cathode design could mitigate the observed limitations and potentially enhance the overall performance of Li- CO_2 batteries [106].

4. Conclusion

Our interactive multiscale modeling framework, integrating FEA, MD, and DFT/AIMD, provides comprehensive insights into Li- CO_2 battery electrochemistry. This approach accurately predicts cell performance while considering critical factors such as CO_2 transport, cathode porosity, and $\text{Li}_2\text{CO}_3/\text{C}$ deposition.

DFT/AIMD calculations reveal high electrical conductivity in the cathode catalyst, while MD simulations show favorable electrolyte properties. FEA results demonstrate an exponential decrease in discharge capacity with increasing current density, from 81,570 mAh/g at 0.1 mA/cm² to 6,200 mAh/g at 1 mA/cm², primarily due to CO₂ transport limitations and reduced cathode porosity. Li₂CO₃/C deposit morphology transitions from larger toroidal structures at lower current densities to thin films at higher current densities, significantly impacting performance. The evolution of the overpotential during discharge reflects changing reaction dynamics, while CO₂ concentration variation plays a crucial role in determining battery performance.

Our multiscale approach bridges atomic-level phenomena and cell-level performance, offering unique insights into spatiotemporal evolution of critical battery parameters and reducing the need for extensive prototyping. Future research should focus on enhancing CO₂ transport, mitigating deposit formation, and optimizing cathode designs with large surface areas, optimal pore sizes, and high porosity. This framework accelerates the development of high-performance Li-CO₂ batteries and sustainable energy storage technologies by providing insights into phenomena difficult to observe experimentally in real-time.

CRedit Authorship Contribution Statement

Mohammed Lemaalem, Selva C. Selvaraj, and Naveen K. Dandu: Conceptualization, Visualization, Software, Data Curation, Formal Analysis, Methodology, Writing – Original Draft, Writing – Review & Editing. Ilias Papailias and Arash Namaeighasemi: Methodology, Data Curation, Formal Analysis, Writing – Review & Editing. Larry A. Curtiss and Amin Salehi-Khojin: Supervision, Data Curation, Formal Analysis, Writing – Review & Editing. Anh T. Ngo: Supervision, Conceptualization, Data Curation, Formal Analysis, Investigation, Project Administration, Writing – Review & Editing.

Author Contributions

This work was conceived by A. T. N., M. L., S. C. S., and N. K. D., carried out the calculations, including first-principles DFT, AIMD results, large-scale MD simulations, and Finite Element Analyses. I. P., A. N., L. A. C., and A. S. K. were responsible for the experimental measurements. All authors contributed to the discussion of the results and the final manuscript.

Declaration of Competing Interest

The authors declare that they have no known competing financial interests or personal relationships that could have appeared to influence the work reported in this paper.

Acknowledgements

This work was supported by the Assistant Secretary for Energy Efficiency and Renewable Energy, Office of Vehicle Technologies of the US Department of Energy, through the Battery Materials Research (BMR) program. We gratefully acknowledge the computing resources provided on Bebop, a high-performance computing cluster operated by the Laboratory Computing Resource Center (LCRC) at Argonne National Laboratory.

Appendix A. Supplementary material

Description of the experimental setup; plots of the mean-square displacement of Li^+ , TFSI^- , and CO_2 within the electrolyte obtained from our MD simulations; plots showing the variation of positive electrode over-potential during the discharge process at various current densities as a function of the state of discharge; a table of parameters used in the finite element analysis (FEA); a table of boundary conditions used in FEA; a table of initial values for independent and dependent variables used in FEA; and plots illustrating changes in porosity and volume fraction of deposited species in the cathode throughout the discharge process at different current densities and discharge states.

Data availability

The data that support the plots within this paper and other findings of this study are available from the corresponding author upon reasonable request.

References

- [1] H. Lv, X. L. Huang, X. Zhu, B. Wang, Metal-related electrocatalysts for Li-CO_2 batteries: an overview of the fundamentals to explore future-oriented strategies, *Journal of Materials Chemistry A* 10 (48) (2022) 25406–25430.
- [2] Y. Qiao, J. Yi, S. Wu, Y. Liu, S. Yang, P. He, H. Zhou, Li-CO_2 electrochemistry: a new strategy for CO_2 fixation and energy storage, *Joule* 1 (2) (2017) 359–370.
- [3] A. Ahmadiparidari, R. E. Warburton, L. Majidi, M. Asadi, A. Chamaani, J. R. Jokisaari, S. Rastegar, Z. Hemmat, B. Sayahpour, R. S. Assary, et al., A long-cycle-life lithium- CO_2 battery with carbon neutrality, *Advanced Materials* 31 (40) (2019) 1902518.
- [4] A. Jaradat, M. K. Ncube, I. Papailias, N. Rai, K. Kumar, V. Koverga, R. Y. Nemade, C. Zhang, N. Shan, H. Shahbazi, et al., Fast charge-transfer rates in Li-CO_2 batteries with a coupled cation-electron transfer process, *Advanced Energy Materials* 14 (15) (2024) 2303467.

- [5] A. D. Pathak, P. R. Adhikari, W. Choi, Lithium-CO₂ batteries and beyond, *Frontiers in Energy Research* 11 (2023) 1150737.
- [6] Z. P. Cano, D. Banham, S. Ye, A. Hintennach, J. Lu, M. Fowler, Z. Chen, Batteries and fuel cells for emerging electric vehicle markets, *Nature energy* 3 (4) (2018) 279–289.
- [7] E. R. Ezeigwe, L. Dong, R. Manjunatha, Y. Zuo, S.-Q. Deng, M. Tan, W. Yan, J. Zhang, D. P. Wilkinson, A review of lithium-O₂/CO₂ and lithium-CO₂ batteries: Advanced electrodes/materials/electrolytes and functional mechanisms, *Nano Energy* 95 (2022) 106964.
- [8] Q. Pan, X. Ma, H. Wang, Y. Shu, H. Liu, L. Yang, W. Li, J. Liu, Y. Wu, Y. Mao, et al., Approaching splendid catalysts for Li-CO₂ battery from the theory to practical designing: A review, *Advanced Materials* 36 (38) (2024) 2406905.
- [9] Z. Zhang, X. Xiao, A. Yan, Z. Zhang, P. Tan, Unravelling the capacity degradation mechanism of thick electrodes in lithium-carbon dioxide batteries via visualization and quantitative techniques, *Advanced Functional Materials* (2024) 2407422.
- [10] T. Yao, Z. Xu, T. Hu, K. Hu, X. Cui, L. Shen, High-throughput computation and machine learning prediction accelerating the design of cathode catalysts for Li-CO₂ batteries, *The Journal of Physical Chemistry C* 128 (28) (2024) 11534–11542.
- [11] X. Mu, P. He, H. Zhou, Toward practical Li-CO₂ batteries: Mechanisms, catalysts, and perspectives, *Accounts of Materials Research* (2024).
- [12] Y. Liu, Z. Zhang, J. Tan, B. Chen, B. Lu, R. Mao, B. Liu, D. Wang, G. Zhou, H.-M. Cheng, Deciphering the contributing motifs of reconstructed cobalt (II) sulfides catalysts in Li-CO₂ batteries, *Nature Communications* 15 (1) (2024) 2167.
- [13] Y. Xiao, S. Hu, Y. Miao, F. Gong, J. Chen, M. Wu, W. Liu, S. Chen, Recent progress in hot spot regulated strategies for catalysts applied in Li-CO₂ batteries, *Small* 20 (1) (2024) 2305009.
- [14] S. Sandhiya, P. Elumalai, Compositionally engineered NiCoLDH@ rGO as bifunctional cathode catalyst for rechargeable Li-O₂/Li-CO₂ battery, *Electrochimica Acta* 487 (2024) 144195.
- [15] F. S. Gittleson, W.-H. Ryu, A. D. Taylor, Operando observation of the gold-electrolyte interface in Li-O₂ batteries, *ACS Applied Materials & Interfaces* 6 (21) (2014) 19017–19025.
- [16] X. Sun, X. Mu, W. Zheng, L. Wang, S. Yang, C. Sheng, H. Pan, W. Li, C.-H. Li, P. He, et al., Binuclear Cu complex catalysis enabling Li-CO₂ battery with a high discharge voltage above 3.0 v, *Nature Communications* 14 (1) (2023) 536.

- [17] M. Wang, K. Yang, Y. Ji, X. Liao, G. Zhang, M. G. Masteghin, N. Peng, F. Richheimer, H. Li, J. Wang, et al., Developing highly reversible Li-CO₂ batteries: from on-chip exploration to practical application, *Energy & environmental science* 16 (9) (2023) 3960–3967.
- [18] S. Zhang, L. Sun, Q. Fan, F. Zhang, Z. Wang, J. Zou, S. Zhao, J. Mao, Z. Guo, Challenges and prospects of lithium-CO₂ batteries, *Nano Research Energy* 1 (1) (2022).
- [19] M. Sarkar, R. Hossain, J. Peng, N. Sharma, V. Sahajwalla, Electrochemical compatibility of microzonal carbon in ion uptake and molecular insights into interphase evolution for next-generation Li-Ion batteries, *Advanced Energy Materials* (2024) 2401977.
- [20] L. Ma, A. Wang, S. Zhang, P. Zhang, J. Wang, Unraveling the decomposition mechanism of Li₂CO₃ in the aprotic medium by isotope-labeled differential electrochemical mass spectrometry, *Journal of Energy Chemistry* 73 (10) (2022) 1.
- [21] L. Zhou, H. Wang, K. Zhang, Y. Qi, C. Shen, T. Jin, K. Xie, Fast decomposition of Li₂CO₃/C actuated by single-atom catalysts for Li-CO₂ batteries, *Sci. China Mater* 64 (9) (2021) 2139–2147.
- [22] Y. Jiao, J. Qin, H. M. K. Sari, D. Li, X. Li, X. Sun, Recent progress and prospects of Li-CO₂ batteries: Mechanisms, catalysts and electrolytes, *Energy Storage Materials* 34 (2021) 148–170.
- [23] X. Yu, A. Manthiram, Recent advances in lithium-carbon dioxide batteries, *Small Structures* 1 (2) (2020) 2000027.
- [24] Y. Dou, Z. Xie, Y. Wei, Z. Peng, Z. Zhou, Redox mediators for high-performance lithium-oxygen batteries, *National Science Review* 9 (4) (2022) nwac040.
- [25] W. Li, M. Zhang, X. Sun, C. Sheng, X. Mu, L. Wang, P. He, H. Zhou, Boosting a practical Li-CO₂ battery through dimerization reaction based on solid redox mediator, *Nature Communications* 15 (1) (2024) 803.
- [26] J. Wang, S. Tian, Y. Lin, H. Song, N. Feng, G. Yang, Q. Zhao, Recent advancement in designing catalysts for rechargeable Li-CO₂ batteries, *Catalysis Science & Technology* (2024).
- [27] D. Na, D. Yu, H. Kim, B. Yoon, D. D. Lee, I. Seo, Enhancing the performance and stability of Li-CO₂ batteries through LAGTP solid electrolyte and MWCNT/Ru cathode integration, *Nanomaterials* 14 (23) (2024) 1894.
- [28] Z. Lu, M. Xiao, S. Wang, D. Han, Z. Huang, S. Huang, Y. Meng, A rechargeable Li-CO₂ battery based on the preservation of dimethyl sulfide, *Journal of Materials Chemistry A* 10 (26) (2022) 13821–13828.

- [29] W. Zhang, F. Zhang, S. Liu, W. K. Pang, Z. Lin, Z. Guo, L. Chai, Regulating the reduction reaction pathways via manipulating the solvation shell and donor number of the solvent in Li-CO₂ chemistry, *Proceedings of the National Academy of Sciences* 120 (14) (2023) e2219692120.
- [30] R. Pipes, A. Bhargav, A. Manthiram, Phenyl disulfide additive for solution-mediated carbon dioxide utilization in Li-CO₂ batteries, *Advanced Energy Materials* 9 (21) (2019) 1900453.
- [31] Y. Wu, S. Cao, J. Hou, Z. Li, B. Zhang, P. Zhai, Y. Zhang, L. Sun, Rational design of nanocatalysts with nonmetal species modification for electrochemical CO₂ reduction, *Advanced Energy Materials* 10 (29) (2020) 2000588.
- [32] A. Jaradat, C. Zhang, S. Shashikant Sutar, N. Shan, S. Wang, S. K. Singh, T. Yang, K. Kumar, K. Sharma, S. Namvar, et al., A high-rate Li-CO₂ battery enabled by 2D medium-entropy catalyst, *Advanced Functional Materials* 33 (21) (2023) 2300814.
- [33] Y. Shi, B. Wei, D. Legut, S. Du, J. S. Francisco, R. Zhang, Highly stable single-atom modified mxenes as cathode-active bifunctional catalysts in Li-CO₂ battery, *Advanced Functional Materials* 32 (48) (2022) 2210218.
- [34] C. Guo, F. Zhang, X. Han, L. Zhang, Q. Hou, L. Gong, J. Wang, Z. Xia, J. Hao, K. Xie, Intrinsic descriptor guided noble metal cathode design for Li-CO₂ battery, *Advanced Materials* 35 (33) (2023) 2302325.
- [35] X. Xiao, W. Yu, W. Shang, P. Tan, Y. Dai, C. Cheng, M. Ni, Investigation on the strategies for discharge capacity improvement of aprotic Li-CO₂ batteries, *Energy & Fuels* 34 (12) (2020) 16870–16878.
- [36] W. Yu, N. Deng, Y. Feng, X. Feng, H. Xiang, L. Gao, B. Cheng, W. Kang, K. Zhang, Understanding multi-scale ion-transport in solid-state lithium batteries, *eScience* (2024) 100278.
- [37] S. Rizvi, M. W. Tahir, N. Ramzan, C. Merten, Multiscale-multidomain model order reduction of Lithium-ion batteries for automobile application: A review, *Journal of Energy Storage* 99 (2024) 113390.
- [38] K. Yang, L. Zhang, W. Wang, C. Long, S. Yang, T. Zhu, X. Liu, Multiscale modeling for enhanced battery health analysis: Pathways to longevity, *Carbon Neutralization* (2024).
- [39] G. Li, C. W. Monroe, Multiscale lithium-battery modeling from materials to cells, *Annual review of chemical and biomolecular engineering* 11 (1) (2020) 277–310.
- [40] J. Bao, W. Xu, P. Bhattacharya, M. Stewart, J.-G. Zhang, W. Pan, Discharge performance of Li-O₂ batteries using a multiscale modeling approach, *The Journal of Physical Chemistry C* 119 (27) (2015) 14851–14860.

- [41] M. R. Mehta, K. B. Knudsen, W. R. Bennett, B. D. McCloskey, J. W. Lawson, Li-O₂ batteries for high specific power applications: a multi-physics simulation study for a single discharge, *Journal of Power Sources* 484 (2021) 229261.
- [42] Y. Mukoyama, S. Hanada, T. Goto, S. Nakanishi, Finite element modeling of the cycle characteristics of Li-O₂ secondary batteries considering surface-and solution-route discharge reactions, *The Journal of Physical Chemistry C* 127 (22) (2023) 10459–10469.
- [43] G.-X. Li, V. Koverga, A. Nguyen, R. Kou, M. Ncube, H. Jiang, K. Wang, M. Liao, H. Guo, J. Chen, et al., Enhancing lithium-metal battery longevity through minimized coordinating diluent, *Nature Energy* (2024) 1–11.
- [44] M. Lemaalem, P. Carbonnière, Tunable properties of poly (vinylidene fluoride)-derived polymers for advancing battery performance and enabling diverse applications, *Polymer* 283 (2023) 126218.
- [45] Q. Deng, Y. Yang, W. Zhao, Z. Tang, K. Yin, Y. Song, Y. Zhang, Revealing the construction of cuoce interfacial sites via increased support utilization for enhanced CO₂ electroreduction and Li-CO₂ batteries, *Journal of Colloid and Interface Science* 651 (2023) 883–893.
- [46] R. Car, M. Parrinello, Unified approach for molecular dynamics and density-functional theory, *Physical review letters* 55 (22) (1985) 2471.
- [47] D. Marx, J. Hutter, *Ab initio molecular dynamics: basic theory and advanced methods*, Cambridge University Press, 2009.
- [48] D. Knyazev, P. Levashov, Ab initio calculation of transport and optical properties of aluminum: Influence of simulation parameters, *Computational materials science* 79 (2013) 817–829.
- [49] R. Kubo, *J. phys. soc. jpn.*, *J. Phys. Soc. Jpn* 12 (570) (1957).
- [50] D. Greenwood, *Proc. phys. soc.*, London 71 (1958) 585.
- [51] M. Lemaalem, P. Carbonniere, Effects of solvents on Li⁺ distribution and dynamics in PVDF/LiFSI solid polymer electrolytes: An all-atom molecular dynamics simulation study, *Solid State Ionics* 399 (2023) 116304.
- [52] S. Tovey, F. Zills, F. Torres-Herrador, C. Lohrmann, M. Brückner, C. Holm, Mdsuite: comprehensive post-processing tool for particle simulations, *Journal of Cheminformatics* 15 (1) (2023) 19.
- [53] G. Kresse, J. Hafner, Ab initio molecular dynamics for liquid metals, *Physical review B* 47 (1) (1993) 558.

- [54] G. Kresse, J. Hafner, Ab initio molecular-dynamics simulation of the liquid-metal-amorphous-semiconductor transition in germanium, *Physical Review B* 49 (20) (1994) 14251.
- [55] A. Jain, S. P. Ong, G. Hautier, W. Chen, W. D. Richards, S. Dacek, S. Cholia, D. Gunter, D. Skinner, G. Ceder, et al., Commentary: The materials project: A materials genome approach to accelerating materials innovation, *APL materials* 1 (1) (2013).
- [56] P. E. Blöchl, Projector augmented-wave method, *Physical review B* 50 (24) (1994) 17953.
- [57] J. P. Perdew, K. Burke, M. Ernzerhof, Generalized gradient approximation made simple, *Physical review letters* 77 (18) (1996) 3865.
- [58] K. Burke, J. P. Perdew, Y. Wang, Derivation of a generalized gradient approximation: The PW91 density functional, in: *Electronic Density Functional Theory: recent progress and new directions*, Springer, 1998, pp. 81–111.
- [59] S. Grimme, J. Antony, S. Ehrlich, H. Krieg, A consistent and accurate ab initio parametrization of density functional dispersion correction (dft-d) for the 94 elements h-pu, *The Journal of chemical physics* 132 (15) (2010).
- [60] D. Knyazev, P. R. Levashov, Thermodynamic, transport, and optical properties of dense silver plasma calculated using the GreeKuP code (2019).
- [61] A. P. Thompson, H. M. Aktulga, R. Berger, D. S. Bolintineanu, W. M. Brown, P. S. Crozier, P. J. in't Veld, A. Kohlmeyer, S. G. Moore, T. D. Nguyen, et al., Lammmps-a flexible simulation tool for particle-based materials modeling at the atomic, meso, and continuum scales, *Computer Physics Communications* 271 (2022) 108171.
- [62] W. McDoniel, M. Höhnerbach, R. Canales, A. E. Ismail, P. Bientinesi, LAMMPS'PPPM long-range solver for the second generation xeon phi, in: *International Conference on High Performance Computing*, Springer, 2017, pp. 61–78.
- [63] R. W. Hockney, J. W. Eastwood, *Computer simulation using particles*, crc Press, 2021.
- [64] K. Sprenger, V. W. Jaeger, J. Pfaendtner, The general AMBER force field (GAFF) can accurately predict thermodynamic and transport properties of many ionic liquids, *The Journal of Physical Chemistry B* 119 (18) (2015) 5882–5895.
- [65] A. K. Rappé, C. J. Casewit, K. Colwell, W. A. Goddard III, W. M. Skiff, UFF, a full periodic table force field for molecular mechanics and molecular dynamics simulations, *Journal of the American chemical society* 114 (25) (1992) 10024–10035.

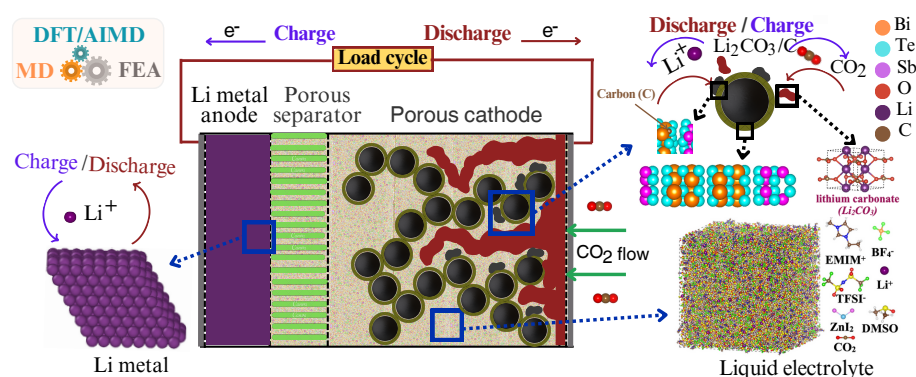
- [66] A. K. Malde, L. Zuo, M. Breeze, M. Stroet, D. Poger, P. C. Nair, C. Oostenbrink, A. E. Mark, An automated force field topology builder (ATB) and repository: version 1.0, *Journal of chemical theory and computation* 7 (12) (2011) 4026–4037.
- [67] M. Stroet, B. Caron, K. M. Visscher, D. P. Geerke, A. K. Malde, A. E. Mark, Automated topology builder version 3.0: Prediction of solvation free enthalpies in water and hexane, *Journal of chemical theory and computation* 14 (11) (2018) 5834–5845.
- [68] K. B. Koziara, M. Stroet, A. K. Malde, A. E. Mark, Testing and validation of the automated topology builder (ATB) version 2.0: prediction of hydration free enthalpies, *Journal of computer-aided molecular design* 28 (3) (2014) 221–233.
- [69] J. N. Canongia Lopes, A. A. Pádua, CL&P: A generic and systematic force field for ionic liquids modeling, *Theoretical Chemistry Accounts* 131 (3) (2012) 1–11.
- [70] K. Goloviznina, Z. Gong, A. A. Padua, The CL&Pol polarizable force field for the simulation of ionic liquids and eutectic solvents, *Wiley Interdisciplinary Reviews: Computational Molecular Science* 12 (3) (2022) e1572.
- [71] A. I. Jewett, D. Stelter, J. Lambert, S. M. Saladi, O. M. Roscioni, M. Ricci, L. Autin, M. Maritan, S. M. Bashusqeh, T. Keyes, et al., Moltemplate: A tool for coarse-grained modeling of complex biological matter and soft condensed matter physics, *Journal of molecular biology* 433 (11) (2021) 166841.
- [72] J. Guérolé, W. G. Nöhring, A. Vaid, F. Houllé, Z. Xie, A. Prakash, E. Bitzek, Assessment and optimization of the fast inertial relaxation engine (fire) for energy minimization in atomistic simulations and its implementation in lammmps, *Computational Materials Science* 175 (2020) 109584.
- [73] A. Dequidt, J. Devemy, A. A. Padua, Thermalized drude oscillators with the lammmps molecular dynamics simulator, *Journal of chemical information and modeling* 56 (1) (2016) 260–268.
- [74] T. J. Barrett, M. L. Minus, Thermostat, barostat, and damping parameter impact on the tensile behavior of graphene, Available at SSRN 4289377 (2023).
- [75] M. Doyle, J. Newman, A. S. Gozdz, C. N. Schmutz, J.-M. Tarascon, Comparison of modeling predictions with experimental data from plastic lithium ion cells, *Journal of the Electrochemical Society* 143 (6) (1996) 1890.

- [76] U. Sahapatsombut, H. Cheng, K. Scott, Modelling the micro-macro homogeneous cycling behaviour of a lithium-air battery, *Journal of Power Sources* 227 (2013) 243–253.
- [77] Y. Mukouyama, S. Hanada, T. Goto, S. Nakanishi, Finite element modeling of the cycle characteristics of Li-O₂ secondary batteries considering surface-and solution-route discharge reactions, *The Journal of Physical Chemistry C* 127 (22) (2023) 10459–10469.
- [78] C. M. Costa, K. J. Merazzo, R. Gonçalves, C. Amos, S. Lanceros-Méndez, Magnetically active lithium-ion batteries towards battery performance improvement, *Iscience* 24 (6) (2021).
- [79] D. A. MacInnes, L. Longworth, Transference numbers by the method of moving boundaries., *Chemical Reviews* 11 (2) (1932) 171–230.
- [80] D. Meng, B. Zheng, G. Lin, M. L. Sushko, Numerical solution of 3d poisson-nernst-planck equations coupled with classical density functional theory for modeling ion and electron transport in a confined environment, *Communications in Computational Physics* 16 (5) (2014) 1298–1322.
- [81] F. L. Usseglio-Viretta, A. Colclasure, A. N. Mistry, K. P. Y. Claver, F. Pouraghajan, D. P. Finegan, T. M. Heenan, D. Abraham, P. P. Mukherjee, D. Wheeler, et al., Resolving the discrepancy in tortuosity factor estimation for Li-ion battery electrodes through micro-macro modeling and experiment, *Journal of The Electrochemical Society* 165 (14) (2018) A3403–A3426.
- [82] L. Holzer, P. Marmet, M. Fingerle, A. Wiegmann, M. Neumann, V. Schmidt, *Tortuosity and microstructure effects in porous media: classical theories, empirical data and modern methods*, Springer Nature, 2023.
- [83] H. J. Goldsmid, Bismuth telluride and its alloys as materials for thermoelectric generation, *Materials* 7 (4) (2014) 2577–2592.
- [84] D. Park, S. Park, K. Jeong, H.-S. Jeong, J. Y. Song, M.-H. Cho, Thermal and electrical conduction of single-crystal Bi₂Te₃ nanostructures grown using a one step process, *Scientific reports* 6 (1) (2016) 19132.
- [85] L.-Y. Lou, J. Yang, Y.-K. Zhu, H. Liang, Y.-X. Zhang, J. Feng, J. He, Z.-H. Ge, L.-D. Zhao, Tunable electrical conductivity and simultaneously enhanced thermoelectric and mechanical properties in n-type Bi₂Te₃, *Advanced Science* 9 (27) (2022) 2203250.
- [86] A. El-Shahat, *Electrical resistivity and conductivity*, BoD-Books on Demand, 2017.
- [87] M. K. Omar, A. H. Ahmad, Electrical impedance spectroscopy and fourier transform infrared studies of new binary Li₂CO₃-LiI solid electrolyte, in: *Materials Science Forum*, Vol. 846, Trans Tech Publ, 2016, pp. 517–522.

- [88] M. Dissanayake, B.-E. Mellander, Phase diagram and electrical conductivity of the $\text{Li}_2\text{SO}_4\text{-Li}_2\text{CO}_3$ system, *Solid State Ionics* 21 (4) (1986) 279–285.
- [89] J. Mizusaki, H. Tagawa, K. Saito, K. Uchida, M. Tezuka, Lithium carbonate as a solid electrolyte, *Solid State Ionics* 53 (1992) 791–797.
- [90] D. Mao, Z. He, W. Lu, Q. Zhu, Carbon tube-based cathode for Li-CO_2 batteries: A review, *Nanomaterials* 12 (12) (2022) 2063.
- [91] Z. Tang, M. Yuan, H. Zhu, G. Zeng, J. Liu, J. Duan, Z. Chen, Promoting the performance of Li-CO_2 batteries via constructing three-dimensional interconnected K^+ doped MnO_2 nanowires networks, *Frontiers in Chemistry* 9 (2021) 670612.
- [92] F. Abild-Pedersen, J. Greeley, F. Studt, J. Rossmeisl, T. R. Munter, P. G. Moses, E. Skulason, T. Bligaard, J. K. Nørskov, Scaling properties of adsorption energies for hydrogen-containing molecules on transition-metal surfaces, *Physical review letters* 99 (1) (2007) 016105.
- [93] A. A. Peterson, F. Abild-Pedersen, F. Studt, J. Rossmeisl, J. K. Nørskov, How copper catalyzes the electroreduction of carbon dioxide into hydrocarbon fuels, *Energy & Environmental Science* 3 (9) (2010) 1311–1315.
- [94] X. Wang, F. Chen, G. M. Girard, H. Zhu, D. R. MacFarlane, D. Mecerreyes, M. Armand, P. C. Howlett, M. Forsyth, Poly (ionic liquid) s-in-salt electrolytes with co-coordination-assisted lithium-ion transport for safe batteries, *Joule* 3 (11) (2019) 2687–2702.
- [95] L. Mohammed, H. Nourddine, D. Abdelali, R. Hamid, et al., Chitosan-covered liposomes as a promising drug transporter: Nanoscale investigations, *RSC advances* 11 (3) (2021) 1503–1516.
- [96] F. S. Gittleson, R. E. Jones, D. K. Ward, M. E. Foster, Oxygen solubility and transport in Li-air battery electrolytes: establishing criteria and strategies for electrolyte design, *Energy & Environmental Science* 10 (5) (2017) 1167–1179.
- [97] R. Evans, G. Dal Poggetto, M. Nilsson, G. A. Morris, Improving the interpretation of small molecule diffusion coefficients, *Analytical chemistry* 90 (6) (2018) 3987–3994.
- [98] J. Li, H. Zhao, H. Qi, X. Sun, X. Song, Z. Guo, A. G. Tamirat, J. Liu, L. Wang, S. Feng, Drawing a pencil-trace cathode for a high-performance polymer-based Li-CO_2 battery with redox mediator, *Advanced Functional Materials* 29 (11) (2019) 1806863.
- [99] Q. Wang, W. Chen, C. Zhao, Z. Li, Analysis of overpotential in discharge process associated with precipitation for vanadium-manganese flow battery, *Journal of Power Sources* 517 (2022) 230717.

- [100] J. Li, A. Dai, K. Amine, J. Lu, Correlating catalyst design and discharged product to reduce overpotential in Li-CO₂ batteries, *Small* 17 (48) (2021) 2007760.
- [101] B. D. Adams, C. Radtke, R. Black, M. L. Trudeau, K. Zaghib, L. F. Nazar, Current density dependence of peroxide formation in the Li-O₂ battery and its effect on charge, *Energy & Environmental Science* 6 (6) (2013) 1772–1778.
- [102] L. D. Griffith, A. E. Sleightholme, J. F. Mansfield, D. J. Siegel, C. W. Monroe, Correlating Li/O₂ cell capacity and product morphology with discharge current, *ACS applied materials & interfaces* 7 (14) (2015) 7670–7678.
- [103] L. Liu, Y. Liu, C. Wang, X. Peng, W. Fang, Y. Hou, J. Wang, J. Ye, Y. Wu, Li₂O₂ formation electrochemistry and its influence on oxygen reduction/evolution reaction kinetics in aprotic li-o₂ batteries, *Small Methods* 6 (1) (2022) 2101280.
- [104] M. Quarti, A. Bayer, W. G. Bessler, Trade-off between energy density and fast-charge capability of lithium-ion batteries: A model-based design study of cells with thick electrodes, *Electrochemical Science Advances* 3 (1) (2023) e2100161.
- [105] X. Xiao, Z. Zhang, P. Tan, Unveiling the mysteries of operating voltages of lithium-carbon dioxide batteries, *Proceedings of the National Academy of Sciences* 120 (6) (2023) e2217454120.
- [106] H. Z. SS, S. Rajendran, A. Sekar, A. Elangovan, J. Li, X. Li, Binder-free Li-O₂ battery cathodes using Ni-and PtRu-coated vertically aligned carbon nanofibers as electrocatalysts for enhanced stability, *Nano Res. Energy* 2 (2023) 9120055.

Graphical abstract



Supporting Information

Interactive Multiscale Modeling to Bridge Atomic Properties and Electrochemical Performance in Li-CO₂ Battery Design

Mohammed Lemaalem^{a,b}, Selva C. Selvaraj^{a,b}, Ilias Papailias^c, Naveen K. Dandu^{a,b}, Arash Namaeighasemi^a, Larry A. Curtiss^b, Amin Salehi-Khojin^c, and Anh T. Ngo^{a,b,}*

^a Department of Chemical Engineering, University of Illinois Chicago, Chicago, IL60608, USA

^b Materials Science Division, Argonne National Laboratory, Lemont, IL 60439, USA.

^c Department of Mechanical Engineering, Lyle School of Engineering, SMU, 3101 Dyer Street

*Corresponding author: anhngo@uic.edu, ango@anl.gov

CONTENTS

1. **Supplementary notes:** Experimental setup.
2. **Figure S1.** Mean-square-displacement of Li^+ , TFSI^- , and CO_2 within the electrolyte obtained from our MD simulation.
3. **Figure S2.** The variation of positive electrode over-potential during the discharge process at various current densities, as a function of the state of discharge.
4. **Table S1.** Parameters used in the finite element analysis (FEA).
5. **Table S2.** Boundary conditions used in FEA.
6. **Table S3.** Initial values of independent and dependent variables used in FEA.
7. **Figure S3.** The change in porosity and volume fraction of the deposited species in the cathode throughout the discharge process at different current densities and discharge states.
8. **Figure S4.** The CO_2 concentration change in the cathode throughout the discharge process at different current densities and discharge states.

1 Supplementary notes

1.1 Experimental setup

1.1.1 Cathode preparation

To synthesize $\text{Sb}_{0.67}\text{Bi}_{1.33}\text{Te}_3$ nanoflakes (NFs), a powder sample weighing 100 mg was dispersed in 20 ml of isopropyl alcohol (IPA) and subjected to ultrasonication for a duration of 24 hours. Subsequently, the solution was centrifuged at 1000 RPM for 15 minutes, allowing for the extraction of the supernatant materials. The resulting $\text{Sb}_{0.67}\text{Bi}_{1.33}\text{Te}_3$ was then

deposited onto carbon cloth with a mass loading of 0.4 mg and subsequently dried under ultraviolet (UV) light.

1.1.2 Electrolyte preparation

A mixture of 1M LiTFSI and 0.025M ZnI₂ was combined with a solution of DMSO and EMIM-BF₄ ionic liquid in a ratio of 3:2. The preparation of the electrolyte was conducted within an argon-filled glove box, maintaining oxygen and humidity levels below 0.1 ppm to prevent contamination.

1.1.3 Three electrodes set up

A three-electrode configuration was employed for conducting electrochemical Linear Sweep Voltammetry (LSV) experiments. The working electrode consisted of Sb_{0.67}Bi_{1.33}Te₃ nanofibers (NFs) coated cathodes, while lithium metal disks served as both the counter and reference electrodes. The electrolyte utilized for the electrochemical measurements was saturated with carbon dioxide (CO₂). The experiments were performed using a Voltalab potentiostat at a sweep rate of 5 mV/s.

1.1.4 Assembly of Li-CO₂ battery

The assembly of the battery was conducted within an argon-filled glove box, maintaining oxygen and humidity levels below 0.1 ppm. The process for assembling the 2032-type coin-cell battery was as follows: (i) the wave spring and spacer were inserted into the coin cell; (ii) a glass-fiber separator, along with 50 μ l of electrolyte, was affixed to the anode; (iii) cathodes coated with Sb_{0.67}Bi_{1.33}Te₃ nanofibers were attached to the separator. Subsequently, holes were drilled, and the case assembly was secured to the top of the cathode. For the battery studies, a Galvanostatic Battery Analyzer (MTI Corp, BST8-MA) was employed. The cycling experiments were conducted within small, sealed bags filled with CO₂ at an ambient temperature of 25 C.

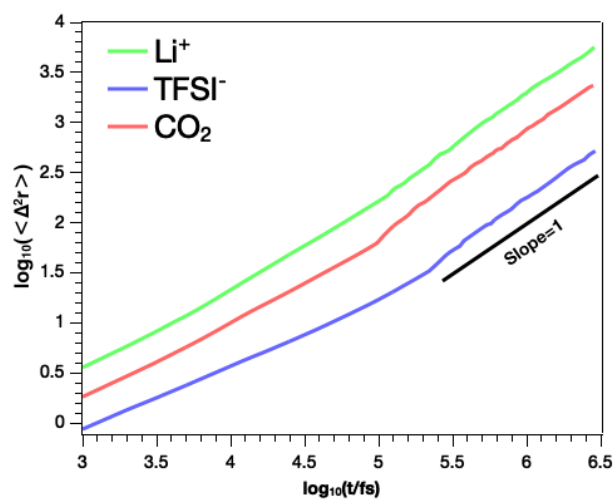


Figure S1: Mean-square-displacement of Li^+ , TFSI^- , and CO_2 within the electrolyte obtained from our MD simulation.

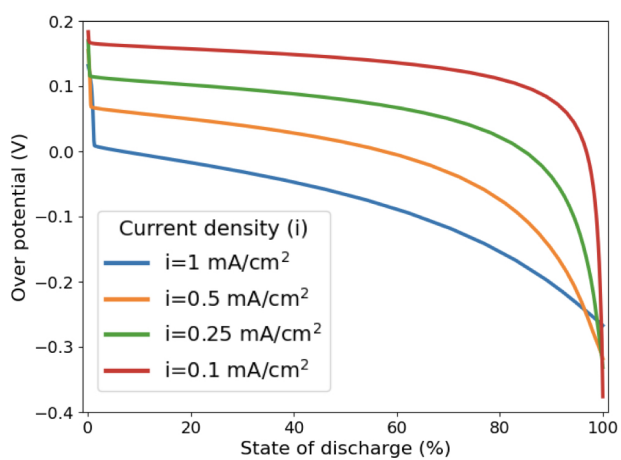


Figure S2: The variation of positive electrode over-potential during the discharge process at various current densities, as a function of the state of discharge.

Table S1: Parameters used in the finite element analysis (FEA).

Symbol	Value	Description
L_{sep}	50 μm	Length of Separator
L_{pos}	2 mm	Length of positive electrode
κ_{pos}	1.4 10^5 S/m	Conductivity of positive electrode
$\epsilon_{l,0}$	0.73	Initial porosity of positive electrode
$\epsilon_{s,0}$	1- $\epsilon_{l,0}$	Initial active material solid fraction of positive electrode
ϵ_{sep}	0.87	Porosity of separator
$r_{pos,0}$	25 nm	Particle radius in the positive electrode
a_0	$3^* \epsilon_{s,0} / r_{pos,0}$	Initial active specific surface area
$\kappa_{Li_2CO_3}$	2 10^{-3} S/m	electrical conductivity of Li_2CO_3 film
$c_{Li,0}$	1000 mol/m ³	Initial concentration of Li^+ in electrolyte
$c_{CO_2,0}$	4.8 mol/m ³	Initial CO_2 concentration in positive electrode
$c_{Li_2CO_3,max}$	0.0371 mol/L	Solubility limit of Li_2CO_3 dissolved in electrolyte
$c_{C,max}$	0 mol/L	Solubility limit of Carbon dissolved in electrolyte
D_{Li^+}	3.17 10^{-9} m ² /s	Diffusion coefficient of Li^+ in electrolyte
D_{CO_2}	1.2 10^{-9} m ² /s	CO_2 diffusion coefficient
σ	6.77 mS/cm	Conductivity of Li^+ in electrolyte
t_+	0.91	Transference number of Li^+ in electrolyte
$d \ln f_{\pm} / d \ln c$	-1.03	Activity dependence
k_a	1.11 10^{-15} m/s	Reaction rate coefficient anodic current
k_c	3.14 10^{-14} m ⁷ /s/mol ²	Reaction rate coefficient cathodic current
$i_{0,Li}$	0.965 A/m ²	Reference exchange current density Li metal
E_{eq1}	2.8 V	Equilibrium potential for CO_2 reduction reaction (discharge)
E_{eq2}	3.8 V	Equilibrium potential for Li_2CO_3 decomposition (charge)
n	2	Number of transferred electrons used to reduce three CO_2 molecules
$\rho_{Li_2CO_3}$	2140 kg/m ³	Density of Li_2CO_3
$M_{Li_2CO_3}$	73.89 10^{-3} kg/mol	Molecular weight of Li_2CO_3
ρ_C	2.11 g/cm ³	Density of carbon
T	300 K	Temperature
$m_{Sb_{0.67}Bi_{1.33}Te_3}$	0.4 mg	mass of active cathode material
A_c	1 cm ²	cross-sectional area

Table S2: Boundary conditions at boundaries 1 ($x=0$), 2 ($x=L_{sep}$), and 3 ($x=L_{sep} + L_{pos}$).

Variable	Value	Boundary
Total current density	\mathbf{i}_{app}	3
\mathbf{c}_{CO_2}	$\mathbf{c}_{CO_2,0}$	3
ϕ_1	0 V	1
∇c_{CO_2}	0	2
$\nabla \mathbf{c}_{Li}$	0	1, 3

Table S3: Initial values of independent and dependent variables.

Variable	Value	Domain
ϕ_1	2.8 V	Porous cathode
ϕ_1	0 V	Separator
ϕ_2	0 V	Porous cathode, Separator
\mathbf{c}_{Li}	$\mathbf{c}_{Li,0}$	Porous cathode, Separator
\mathbf{c}_{CO_2}	$\mathbf{c}_{CO_2,0}$	Porous cathode
$\mathbf{c}_{Li_2CO_3}$	$\mathbf{c}_{Li_2CO_3,max}$	Porous cathode
\mathbf{c}_C	$\mathbf{c}_{C,max}$	Porous cathode
ϵ	$\epsilon_{l,0}$	Porous cathode

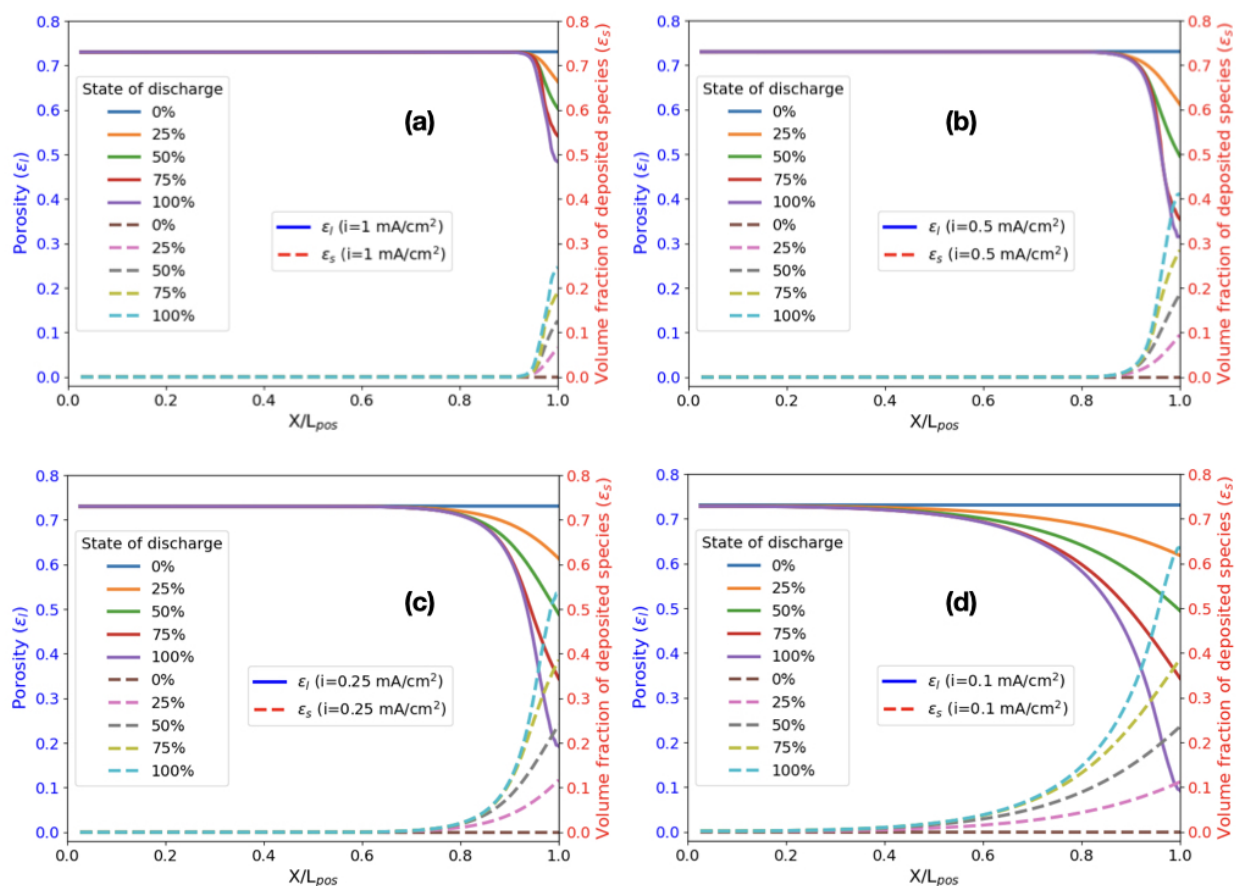


Figure S3: The change in porosity and volume fraction of deposited species in the cathode throughout the discharge process at different current densities ((a) 1, (b) 0.5, (c) 0.25, and (d) 0.1 mA/cm²) in relation to the state of discharge. The distance (x) is normalized by the cathode length (L_{pos}).

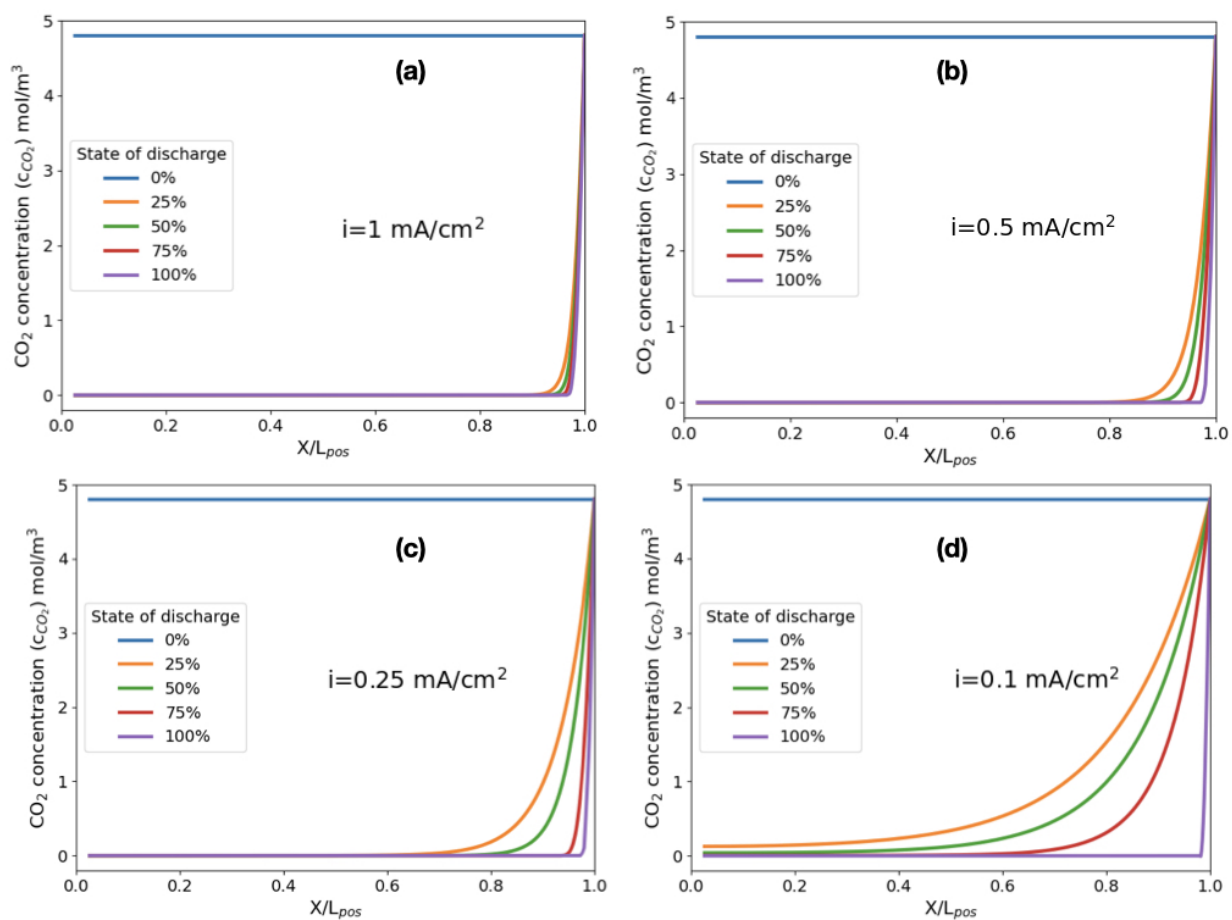


Figure S4: The local CO₂ concentration within the Li-CO₂ cathode during discharge was analyzed at various rates of 0.1, 0.25, 0.5, and 1 mA/cm², corresponding to different discharge levels (0 % indicates a fully charged battery). The distance (X) is normalized by the cathode length (L_{pos}).